Research Square

Preprints are preliminary reports that have not undergone peer review.
They should not be considered conclusive, used to inform clinical practice,
or referenced by the media as validated information.

# Practical formulas for additive manufacturing alloys: thermophysical and mechanical properties

**Vitaliy Gilmutdinov**

vital@udman.ru

Udmurt Federal Research Center of the Ural Branch of RAS

**Rinetta Mosina**

Udmurt State University

**Georgii Gordeev**

Udmurt State University

**Vladimir Ankudinov**

Udmurt State University

**Igor Kuzmin**

Udmurt State University

**Mikhail Krivilyov**

Udmurt Federal Research Center of the Ural Branch of RAS

**Research Article**

**Keywords:** properties, temperature dependence, SS316L, Ti–6Al–4V, Inconel 718

**Posted Date:** August 3rd, 2026

**DOI:** https://doi.org/10.21203/rs.3.rs-10433902/v1

**License:** This work is licensed under a Creative Commons Attribution 4.0 International License.
Read Full License

**Additional Declarations:** No competing interests reported.

# Practical formulas for additive manufacturing alloys: thermophysical and mechanical properties

**Abstract**

Accurate thermophysical and mechanical property data are essential for reliable implementation of laser powder bed fusion and directed energy deposition. However, these data for alloys crucial in additive manufacturing remain scattered across handbooks and original studies. They are often measured under non-AM-specific conditions, lacking unified temperature-dependent formulations. In this work, explicit formulas for the thermophysical and mechanical characteristics of SS316L, Ti-6Al-4V and Inconel 718 alloys as a function of temperature have been derived. The proposed expressions are obtained through critical review and statistical analysis of over 100 experimental datasets and well-established theoretical models, covering temperatures from room temperature to above the melting point. Overall, eleven characteristics are described, including density, enthalpy, heat capacity, thermal conductivity, electrical resistivity, surface tension, viscosity, Young's and shear moduli, Poisson's ratio, and yield strength. An original approach is proposed that accounts for the effect of residual porosity on the material properties of 3D-printed samples. The proposed correlations show fair agreement with reference experimental data, with typical deviations within $\pm 10\%$ for most properties. In contrast to existing property databases, the temperature-dependent polynomials are directly compatible with finite element and computational fluid dynamics simulation frameworks. The property models are relevant for predicting melt pool dynamics, thermal stress evolution, and defect formation, including keyhole porosity and spattering, which are critical for

process optimization. The provided tabular data and analytical formulas can be used for simulation and optimization of processing regimes in 3D metal additive manufacturing.

**Keywords:** properties, temperature dependence, SS316L, Ti–6Al–4V, Inconel 718

# 1 Introduction

Thermophysical and mechanical properties of steels and other industrial alloys have always been intensively studied in mechanical and materials engineering. Various materials with application-specific characteristics are used in aerospace technology, power engineering, and healthcare. As an example, stainless steel 316L (SS316L) is used broadly in the food, chemical, and atomic power domains. The titanium Ti–6Al–4V alloy is indispensable in the manufacturing of aerospace assemblies and high-pressure tanks employed at variable temperatures. The nickel Inconel 718 superalloy is recognized in the production of hot-zone turbines and their blades. Also, its application includes the construction of nuclear power reactors and machinery in the oil and gas industries.

Additive manufacturing (AM) of metals [1–4] has been developing for decades and now it has reached a mature stage sufficient for its effective utilization in industry. One of the distinctive features is the possibility of 3D-printing of parts with the controlled structure, complex internal geometry, and inner channels. Among a wide range of specific AM methods, laser powder bed fusion (PBF-LB), directed energy deposition (DED), and their variations exhibit a strong dependence on temperature. In these processes, the consequent stages of heating, melting, consolidation, and solidification of powder particles are conjugated with solid-phase and liquid-to-solid transitions. Accounting for a short (of about 100 ms) thermal cycle of local treatment, proper assessment of thermophysical properties as a function of temperature is vital for metal

AM. Other parameters like pressure, processing regimes, and residual porosity may also affect the final characteristics.

Draft analysis of available literature data reveals that the property–temperature relationships often show nonmonotonic behavior, discontinuity of the first derivative, and other features. This is typical for multi-component alloys with phase transitions and the presence of polyvalent metals. Hence, it may cause the formation of defects, especially if an unstable PBF-LB or DED processing regime is implemented. The most difficult and challenging problem is a substantial dependence of the surface tension $\gamma$ on the content of sulfur and other impurities. For instance, in SS316L, sulfur has a strong impact not only on $\gamma$ itself but also on its first derivative $d\gamma/dT$ with respect to temperature. Consequently, the sign of $d\gamma/dT$ alters the Marangoni coefficient (see [5, 6] and references therein). For Ti–6Al–4V and Inconel 718 alloys, experiments show a complex temperature dependence of the thermal conductivity $k$ owing to polymorphic transformations. As a result, no simple approximation of $k(T)$ by a set of piecewise continuous curves exists (see [7]).

It is worth mentioning several additional problems with the values of the thermophysical properties of metallic materials. (i) Alloys exhibit inhomogeneous microstructures that complicate the formulation of clear and representative data [8–11]. (ii) Thermophysical properties vary as a function of temperature non-linearly; hence, more accurate thermal control is required in measurements. (iii) Different measurement techniques may contradict each other; thus, the correct estimation of values may be difficult. (iv) In the case of complex experimental conditions such as in additive manufacturing, the influence of processing parameters [12–14] can be properly accounted for only with the assistance of multi-physics simulations [13, 15]. The current state of research shows a large variety of possible multiscale approaches to get decent quantitative estimates in powder sintering experiments [14, 16–19]. The continuous media approach tends to be a productive and precise method [20–22], but the models

are highly dependent on the values of effective physical characteristics. Therefore, the need for the data presented in the present work is high in the AM domain.

The next feature of AM comes from the process of powder melting and its deposition, which implies the analysis of underlying phenomena in their full complexity. In the formed multi-phase system, the gas, liquid, and solid phases interface with each other. Hence, substantial porosity may develop, which affects the thermophysical properties. Usually, the structure of powders is complex because of a wide spread of particle sizes and the irregular morphology of pores in individual particles [23–25]. Thus, the detailed prediction of the effective thermal conductivity of powders requires consideration of (i) the shape and size distribution, (ii) the conductivity of particles and the gas atmosphere, and (iii) heat transfer between the metal and gas phases [26]. Therefore, the most comprehensive approach should combine two different methods [27]: the classic packed bed approach [23, 26, 28] and stochastic random filling models (see [24] and references therein).

For better accuracy and confidence, different experimental techniques have recently been developed and cross-validated. Thermophysical measurements are conducted via differential scanning calorimetry and dilatometry [7, 29–32], extended with local heating by short laser pulses [7, 32–35]. The latter method provides local and effective heating of the material to high temperatures. In viscosity and surface tension measurements, a few methods are widely used, including the oscillating vessel technique [36], the levitated drop method [36–38], the oscillating drop method in parabolic microgravity flights [39, 40], and containerless electromagnetic levitation onboard the International Space Station (ISS) [41, 42]. Many outstanding scientists have already contributed to this domain of research. Their work delivered the accurate thermophysical data to multiple datasets widely accessible online. In the present paper, we may highlight and cite only some papers and books, including widely cited studies by K.C. Mills [43] and Y.S. Touloukian [44], as well as IAEA reports [45]. The modern

input of the research groups under the guidance of NIST, NASA, ESA, Roscosmos, and JAXA is greatly appreciated.

Experimental assessment of mechanical and granulometric properties is performed with different techniques, including various tension tests [46, 47], scanning electron microscopy [48], ultrasonic testing (UT) [49, 50], compression tests [51], X-ray computed tomography [52], impulse excitation technique [53], and others. In solid mechanics, computer simulations are often complemented by laboratory tests for the analysis of non-linear material response. To that end, computational methods based on finite element discretization [54] are matched with constitutive models of solid mechanics [55].

The main objective of this paper is as follows. In literature, an extensive data set with the thermophysical properties of SS316L, Ti–6Al–4V and Inconel 718 is provided [6, 7, 31, 33–35, 37–45, 56–72]. Often, the data are scattered over multiple publications and valid for limited temperature intervals according to measurement performed by the authors. In this work, the authors aim to classify and cross-validated the properties of SS316L, Ti–6Al–4V and Inconel 718 that are important for AM. To that end, the following steps are performed: (i) review and critical assessment of experimental data available in papers and handbooks, (ii) correlation and regressive analysis, (iii) development of explicit formulas for piecewise continuous approximations of properties as functions of temperature and porosity. Thus, the practical importance and scientific novelty are given by the applicability of the derived formulas in the wide temperature interval between the room and boiling temperatures. Moreover, the temperature range near the melting temperature is thoroughly described both in the solid and liquid phases.

## 2 Methodology

A common method for assessing measured experimental data is correlation-regression analysis. First, it evaluates the level of correlation between two or more characteristics. Then, in case of mutual correlation, a functional relation between them is derived as a closed-form expression that includes the independent parameters of the system under consideration. For better representation, both interpolation and extrapolation techniques are widely used. In the present paper, an extended set of experimental and simulation data available in the literature on the chosen alloys was used [6, 7, 31, 33–35, 37–45, 59–72]. The least-squares procedure and radial basis function method are both used for the construction of the final expressions of properties as functions of temperature. The list of all thermophysical and mechanical properties assessed in the paper with the derivation of the closed-form expressions is provided in Table 1.

**Table 1**: List of thermophysical and mechanical properties assessed in the paper with the derivation of closed-form expressions over a wide temperature range.

| **Parameter name** | **Symbol** | **Unit** |
|---|---|---|
| Density | $\rho$ | kg m$^{-3}$ |
| Heat capacity at constant pressure | $c_p$ | J kg$^{-1}$ K$^{-1}$ |
| Thermal conductivity | $k$ | W m$^{-1}$ K$^{-1}$ |
| Enthalpy | $\Delta H$ | kJ kg$^{-1}$ |
| Electrical resistivity | $\rho_{\mathrm{el}}$ | $\Omega$ m |
| Dynamic viscosity | $\mu$ | Pa s |
| Liquid-gas surface tension | $\gamma$ | N m$^{-1}$ |
| Young's modulus | $E$ | Pa |
| Shear modulus | $G$ | Pa |
| Poisson's ratio | $\nu$ | – |
| Yield strength | $\sigma_{0.2}$ | Pa |

For the heat transport coefficients, we combine the analytical models suggested by different authors [24, 26, 28, 73] with the results of numerical simulations [27]. The temperature-dependent coefficients are introduced into the transport models in

the quasi-continuous approach for partially melted and dry powders, allowing one to determine their thermal and mechanical properties considering them as multiphase media. The evaluation procedure for the effective mechanical properties of porous materials is based on standard constitutive models of solid mechanics averaged over the representative volume. Owing to a high difference in elasticity between the solid matrix and voids, well-established techniques for composite materials like the Eshelby and Mori-Tanaka models are not directly applicable. Instead, a homogenization method for strain averaging is employed. Several models comply with this principle and have been used here, including the Voigt-Reuss and Hashin-Shtrikman bounds, Christensen, Wachtman, and Mechanical Threshold Stress models [74–76].

Some properties of solids conform with the lever rule (sometimes referred to in the literature as the rule of mixtures). This approach is based on the assumption that specific thermophysical characteristics, such as density or specific heat, are linear functions of their constituents' properties according to:

$$\rho(T) = \sum_{i=1}^{N} x_i \rho_i(T), \tag{1}$$

$$c_p(T) = \sum_{i=1}^{N} x_i c_{p,i}(T), \tag{2}$$

where $x_i$ is the mass (or volumetric, depending on the definition) fraction of the component in a mixture, while $\rho_i$ and $c_{p,i}$ are the density and specific heat of the $i$-th component, respectively. The temperature dependencies of density and specific heat for individual chemical elements are taken from [72].

The mechanical properties are mutually related through the elastic relationships:

$$
\begin{aligned}
K &= \lambda + \frac{2}{3}G = \frac{E}{3(1-2\nu)}, \\
G &= \frac{3KE}{9K-E} = 3\frac{K-\lambda}{2} = \frac{E}{2(1+\nu)}, \\
E &= \frac{9KG}{3K+G} = 2G(1+\nu), \\
\nu &= \frac{3K-2G}{6K+2G} = \frac{E}{2G} - 1,
\end{aligned}
\tag{3}
$$

where $K$, $G$, $E$, $\nu$, and $\lambda$ represent the bulk modulus of linear elasticity, shear modulus, Young's modulus, Poisson's ratio, and the Lamé multiplier, respectively.

The construction of analytical models for the practical calculation of material properties is performed through a multi-step algorithm. This includes a preliminary confidence analysis of available data followed by a search for their optimal power expansion as a function of governing parameters. The applied approach consists of the following steps:

***Step 1: Data compilation.*** Data collection is performed using available literature sources, internal experimental tests, and theoretical models suggested in scholarly works. At this stage, emphasis is placed on gathering empirical data provided by different experimental techniques to ensure robust cross-validation.

***Step 1: Confidence evaluation.*** Evaluation of the retrieved datasets based on confidence criteria. Here, a key metric is the reproducibility of the same functional dependency of the selected property during analysis within finite parameter intervals. A significant deviation within the collected datasets is occasionally considered acceptable. Some properties, such as surface tension, are reported in the literature with

contradictory functional trends due to the effect of dissolved impurities. For these scenarios, all datasets are retained in the analysis to allow an independent assessment of property variability by the readers.

***Step 3: Selection of the regressive model.*** Selection of the regressive model as a power expansion of governing parameters. To that end, different power terms are combined for the most accurate representation of the retrieved empirical data. Often, the observed functional dependencies are non-monotonic and may exhibit inflections. Under such circumstances, a piecewise approximation by continuous functions is used, allowing for a discontinuity of the first derivative between intervals, while the continuity of the approximated function itself is strictly preserved.

**Note 1 to Step 3:** The required accuracy of the expansion coefficients is property-specific and cannot be unified. Therefore, the precision of the coefficients, defined by the number of digits after the decimal point, is chosen to achieve fair agreement with the verification data.

**Note 2 to Step 3:** The construction of regressive models for mechanical properties as functions of temperature is performed using the Akaike information [77], Bayesian information [78], and Hannan-Quinn [79] criteria (AIC, BIC, and HQC, respectively). These criteria are not employed for the analysis of thermophysical properties because their temperature dependence is usually complex and non-linear. To incorporate these complex functional dependencies, these properties are better approximated using a piecewise approach.

***Step 4: Verification of convergence.*** The divergence between the regressive model and empirical data is calculated using the $L_2$-norm according to:

$$\varepsilon = \|\mathbf{x}_{\text{model}} - \mathbf{x}_{\text{emp. data}}\|_2 = \sqrt{\sum_{i=1}^{N} \left(x_i^{\text{model}} - x_i^{\text{emp. data}}\right)^2}. \tag{4}$$

The relative data validity within 10% is assumed to be acceptable. For the final confirmation of the model, correspondence with at least two datasets is required. Among

the available empirical data, publications reporting datasets obtained via modern measurement techniques are prioritized. The year of publication is also accounted for in the approach implemented in this paper. Table 3 provides the chemical compositions of the alloys selected for analysis. Table 2 collects their reference thermophysical and mechanical properties at room and melting temperatures.

The next sections present the results of the present study according to the following structure. Each property is considered in a separate section. First, the fundamental definition of the chosen property is provided. Next, the recommended analytical and regressive models with their expansion coefficients are presented. Then, the plots of the selected regressive model combined with verification data are drawn for all studied materials. Finally, specific features of the analyzed property are discussed. The section "Supplementary materials" contains the tabular data for all thermophysical and mechanical properties of SS316L, Ti–6Al–4V, and Inconel 718 as a function of temperature.

**Table 2**: Reference thermophysical and mechanical properties at room and melting temperatures collected from relevant publications on material properties. $NTP$ denotes normal temperature and pressure conditions equal to 298.15 K and 101325 Pa according to NIST.

| **Parameter name** | **Symbol** | **SS316L** | **Ti–6Al–4V** | **Inconel 718** | **SI unit** |
|---|---|---|---|---|---|
| Boiling temperature | $T_{\text{boil}}$ | 3100 | 3550 | 3100 | K |

continued on next page

Table 2 – continued

| **Parameter name** | **Symbol** | **SS316L** | **Ti–6Al–4V** | **Inconel 718** | **SI unit** |
|---|---|---|---|---|---|
| Melting temperature (liquidus) | $T_m$ | 1713 | 1921 | 1609 | K |
| Solidification temperature (solidus) | $T_{\text{sol}}$ | 1679 | 1878 | 1533 | K |
| Heat of fusion | $L_{\text{melt}}$ | $2.70 \times 10^5$ | $2.82 \times 10^5$ | $2.27 \times 10^5$ | J kg$^{-1}$ |
| Heat of boiling | $L_{\text{boil}}$ | $7.45 \times 10^6$ | $9.83 \times 10^6$ | $7.34 \times 10^6$ | J kg$^{-1}$ |
| Radiative emissivity | $\varepsilon_{\text{rad}}$ | 0.4 | 0.4 | 0.4 | – |
| Laser absorptivity by the solids | $A_{\lambda,\text{solid}}$ | 0.55 | 0.35 | 0.45 | – |
| Laser absorptivity by the melt | $A_{\lambda,\text{melt}}$ | 0.3 | 0.35 | 0.45 | – |
| Density (at NTP) | $\rho$(NTP) | 8000 | 4432.1 | 8190 | kg m$^{-3}$ |

continued on next page

Table 2 – continued

| **Parameter name** | **Symbol** | **SS316L** | **Ti–6Al–4V** | **Inconel 718** | **SI unit** |
|---|---|---|---|---|---|
| Density (at $T_m$) | $\rho(T_m)$ | 6954 | 4086 | 7390 | kg $m^{-3}$ |
| Specific heat (at NTP) | $c_p$(NTP) | 463.928 | 525.04 | 720 | J $kg^{-1}$ $K^{-1}$ |
| Specific heat (at $T_m$) | $c_p(T_m)$ | 735 | 855 | 720 | J $kg^{-1}$ $K^{-1}$ |
| Thermal conductivity (at NTP) | $k$(NTP) | 13.24 | 7.0398 | 9.94 | W $m^{-1}$ $K^{-1}$ |
| Thermal conductivity (at $T_m$) | $k(T_m)$ | 30 | 28.5 | 29.6 | W $m^{-1}$ $K^{-1}$ |
| Viscosity (at $T_m$) | $\mu(T_m)$ | 0.0075 | 0.0083 | 0.0072 | Pa s |
| Melt-gas surface tension (at $T_m$) | $\gamma(T_m)$ | 1.67 | 1.461 | 1.882 | N $m^{-1}$ |

continued on next page

Table 2 – continued

| **Parameter name** | **Symbol** | **SS316L** | **Ti–6Al–4V** | **Inconel 718** | **SI unit** |
|---|---|---|---|---|---|
| Temperature coeff. of surface tension | $d\gamma/dT$ | 0.0004 | −0.0004 | −0.00037 | $\mathrm{N\,m^{-1}\,K^{-1}}$ |
| Electrical resistivity (at NTP) | $\rho_{\mathrm{el}}$(NTP) | 0.75 | 1.71 | 1.182 | $\mu\Omega\,\mathrm{m}$ |
| Yield stress 0.2 (at NTP) | $\sigma_{0.2}$(NTP) | $3.80 \times 10^8$ | $8.80 \times 10^8$ | $1.20 \times 10^9$ | Pa |
| Tensile stress (at NTP) | $\sigma_{\mathrm{UTS}}$(NTP) | $5.85 \times 10^8$ | $4.82 \times 10^8$ | $1.38 \times 10^9$ | Pa |
| Young modulus (at NTP) | $E$(NTP) | $1.93 \times 10^{11}$ | $1.14 \times 10^{11}$ | $2.05 \times 10^{11}$ | Pa |
| Shear modulus (at NTP) | $G$(NTP) | $7.30 \times 10^{10}$ | $4.21 \times 10^{10}$ | $7.72 \times 10^{10}$ | Pa |
| Poisson's ratio (at NTP) | $\nu$(NTP) | 0.33 | 0.339 | 0.294 | – |

**Table 3**: Chemical composition (in wt.%) of stainless steel 316L, titanium Ti–6Al–4V alloy, and nickel Inconel 718 superalloy [43, 45, 65].

| **SS316L** | | | | | | | | |
|---|---|---|---|---|---|---|---|---|
| **C** | **Cr** | **Cu** | **Fe** | **Mn** | **Mo** | **Ni** | **Si** | **S** |
| 0.08 | 16–18 | 0.3 | 65 | 2.0 | 2.5 | 10–14 | 1 | $\leq 0.03$ |

| **Ti–6Al–4V** | | | | | | | |
|---|---|---|---|---|---|---|---|
| **Al** | **C** | **Fe** | **H** | **N** | **O** | **V** | **Ti** |
| 5.5–6.7 | 0.1 | 0.4 | 0.015 | 0.05 | 0.2 | 3.5–4.5 | balance |

| **Inconel 718** | | | | | | | | | |
|---|---|---|---|---|---|---|---|---|---|
| **C** | **Ni** | **Cr** | **Ti** | **Al** | **Mn** | **Fe** | **Mo** | **Nb** | **Si** |
| 0.10 | 55 | 21 | 1.15 | 0.8 | 0.35 | 12.5 | 3.3 | 5.5 | 0.35 |

# 3 Results and discussion

## 3.1 Density $\rho$

The density of metallic alloys governs several "process–structure–property" relationships important in additive manufacturing. On the one hand, alloy density influences thermal regimes because materials with higher density typically exhibit better thermal conductivity [24], supporting more efficient heat dissipation during laser processing. This eventually reduces the thermal distortion [13] of printed parts. High density also leads to a reduction in the formation of voids and porosity as a result of an improved consolidation rate and a decrease in gas trapping [80]. Dense powder particles are less affected by aerodynamic effects during DED deposition [81–83], which favors a more uniform material flux. On the other hand, alloys with higher density require extra energy for melting, which affects the overall energy balance of the process.

For multi-phase media, the effective density is usually defined by integrating the mass over a representative volume element. The effective density of porous powders and sintered materials processed by PBF-LB in a protective gas atmosphere can be calculated using a linear approximation [27]:

$$\rho_{\text{eff}}(T) = \rho_{\text{metal}}(T)(1-\varepsilon) + \rho_{\text{gas}}(T)\varepsilon, \tag{5}$$

where $\rho_{\text{metal}}$ is the temperature-dependent density of the metal, $\rho_{\text{gas}}$ is the density of the atmosphere, and $\varepsilon$ is the local porosity. For the calculation of the gas density, the virial equation for gases [84, 85] can be employed as:

$$\frac{p}{RT\rho_{\text{gas}}} = A + B\rho_{\text{gas}} + C\rho_{\text{gas}}^2 + \ldots, \tag{6}$$

where $p$ is the gas pressure, $R = 8.314$ J mol$^{-1}$ K$^{-1}$ is the universal gas constant, $\rho_{\text{gas}}$ is the density of the gas, and $A, B, C \ldots$ are the virial coefficients explicitly determined for specific gases [86, 87]. The density of a typical shielding gas in PBF-LB processing at a flow rate of 4 m/s and an overpressure around 10 mbar [88] differs by three orders of magnitude compared to $\rho_{\text{metal}}$, which is typical even for light alloys. A fair approximation valid for the majority of calculations is to discard the gas density, yielding an effective density of $\rho_{\text{eff}} \approx \rho_{\text{metal}}(1-\varepsilon)$. In contrast to density, heat transfer via gas pores cannot be neglected [27, 88], and this contribution is retained in the thermal conductivity section.

The density of bulk metallic materials is fairly well approximated by a quasi-linear function of temperature within a specific polymorphic phase:

$$\rho_{\text{metal}}(T) = a + bT + cT^2, \quad \text{with} \quad cT^2 \ll bT, \tag{7}$$

where the quadratic term $cT^2$ is significantly less valuable in comparison to $bT$. A typical linear crossover in $\rho_{\text{metal}}(T)$ is always observed between the solidus and liquidus temperatures, where the density decreases by up to 10% during alloy melting. This density jump between the solid and liquid phases is specific to first-order phase transitions.

All alloys considered here do not reveal any anomalous features in their density as a function of temperature $\rho_{\text{metal}}(T)$. Therefore, the coefficients $a$, $b$, and $c$ in Eq. (7) are introduced as constants within each temperature interval. The density data are depicted below in Fig. 1 along with a set of references, which are provided in the right panel with the corresponding experimental methods used to obtain these results. The characteristic solidus $T_{\text{sol}}$ and liquidus $T_m$ temperatures are designated by vertical lines. They correspond to the bounds of the second polynomial range for each material

(see Eq. (7) and the corresponding coefficients in Table 4). The solid black line represents the approximation proposed in the present work, expressed through a piecewise continuous polynomial by Eq. (7), where the coefficients at powers of $T$ are given for the valid temperature ranges for each material in Table 4.

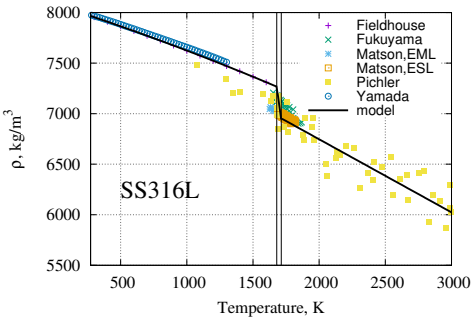
**Table 4**: Polynomial expansion coefficients derived for the density $\rho(T)$ (kg m$^{-3}$) of SS316L, Ti–6Al–4V, and Inconel 718 for given temperature ranges.

| **Temperature range (K)** | $a$ $[T^0]$ | $b$ $[T^1]$ | $c$ $[T^2]$ |
|---|---|---|---|
| *SS316L* | | | |
| $T < 1679$ | $8.084 \times 10^3$ | $-4.209 \times 10^{-1}$ | $-3.894 \times 10^{-5}$ |
| $1679 \leq T \leq 1713$ | $2.31888 \times 10^4$ | $-9.48258$ | 0 |
| $T > 1713$ | $8.119228 \times 10^3$ | $-7.22938 \times 10^{-1}$ | 0 |
| *Ti–6Al–4V* | | | |
| $T < 1878$ | $4.465892 \times 10^3$ | $-1.54 \times 10^{-1}$ | 0 |
| $1878 \leq T \leq 1921$ | $8.10615 \times 10^3$ | $-2.09237$ | 0 |
| $T > 1921$ | $4.955 \times 10^3$ | $-4.52 \times 10^{-1}$ | 0 |
| *Inconel 718* | | | |
| $T < 1533$ | $8.32134 \times 10^3$ | $-4.40753 \times 10^{-1}$ | 0 |
| $1533 \leq T \leq 1609$ | $1.28028 \times 10^4$ | $-3.36408$ | 0 |
| $T > 1609$ | $8.21546 \times 10^3$ | $-5.13027 \times 10^{-1}$ | 0 |

## 3.2 Specific enthalpy $\Delta H_\mathrm{f}$ and latent heat of fusion $L_\mathrm{melt}$

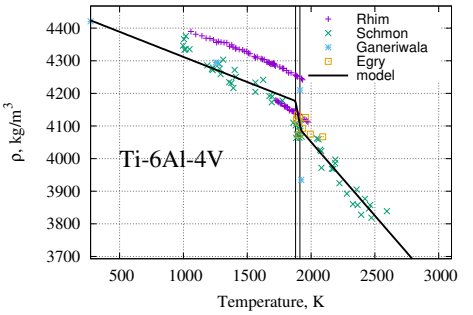
Enthalpy $H(T) = U(T) + pV$ is a thermodynamic quantity that describes the internal energy $U$ of a system coupled with its potential energy $pV$. The specific heat capacity $c_p$, considered further in Sec. 3.3, is the partial derivative of enthalpy at constant pressure $p$, defined as $c_p = (\partial H/\partial T)_p$. For practical purposes, enthalpy is evaluated through its increment relative to a reference state value $H_0$ as:

$$\Delta H(T) = H(T) - H_0, \quad \text{where} \quad H_0 = H|_{T=298\,\mathrm{K}}. \tag{8}$$



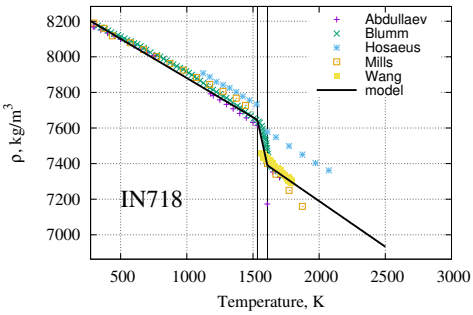

(a) SS316L stainless steel

**References**
Fieldhouse (linear thermal expansion) [89], Fukuyama (DSC, electromagnetic levitation, oscillating drop) [65], Pichler (ohmic pulse-heating, DSC) [68], Yamada [90], and Matson (electrostatic/electromagnetic levitation on ISS) [41].




(b) Ti–6Al–4V

**References**
Rhim (electrostatic levitation) [91], Schmon (pulse-heating) [92], Ganeriwala (modeling, Diablo code [93]) [94], and Egry (levitated drop, electromagnetic levitation) [63].




(c) Inconel 718

**References**
Abdullaev (dilatometer, gamma-ray attenuation) [95], Blumm (dilatometer) [96], Hosaeus (resistive heating) [31], Mills (review) [43], and Wang (electrostatic levitation) [97].

**Figure 1**: Temperature dependence $\rho(T)$ of density derived for (a) SS316L stainless steel, (b) Ti–6Al–4V, and (c) Inconel 718 alloys. The solidus $T_{\mathrm{sol}}$ and liquidus $T_m$ temperatures are designated by vertical lines.

The experimentally measured temperature dependence of $\Delta H(T)$ combines intervals of steep monotonic increases and flat phase-change plateaus. Therefore, a comprehensive approximation of $\Delta H(T)$ is provided by a piecewise continuous polynomial that includes both integer and fractional powers as follows:

$$\Delta H(T) = a + bT^{0.25} + cT^{0.5} + dT + eT^2 + fT^3 + gT^4 + hT^5. \tag{9}$$

The coefficients of this expansion for the studied alloys are summarized in Table 5, whereas Fig. 2 illustrates the continuous $\Delta H(T)$ functions constructed for all analyzed materials.

The latent heat of fusion $L_{\text{melt}}$, also referred to in the literature as the specific enthalpy of fusion $\Delta H_{\text{f}}$, is the net enthalpy change occurring between the solidus and liquidus temperatures, expressed as:

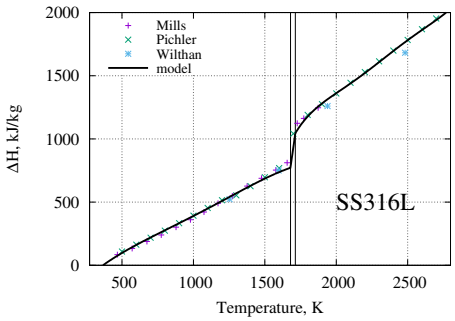
$$L_{\text{melt}} \equiv \Delta H_{\text{f}} = \Delta H(T_m) - \Delta H(T_{\text{sol}}). \tag{10}$$

In this context, $L_{\text{melt}}$ represents the latent heat or thermal energy absorbed or released during the liquid-to-solid phase transition per unit mass. These latent heat values have been summarized previously in Table 2 of Section 2.

Furthermore, the effective latent heat of fusion $L_{\text{melt}}$ for porous media is treated as an additive physical parameter, analogous to density or mass. In a powder bed or a sintered porous component, the volume-averaged enthalpy depends on the volume fraction of the solid metallic matrix and voids, which is defined by the local porosity $\varepsilon$ as:

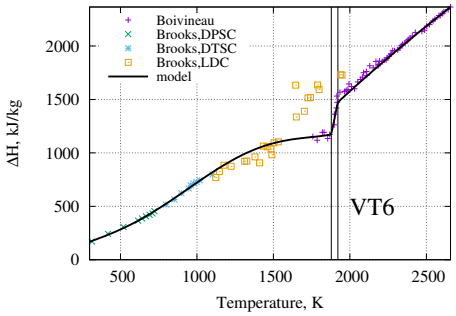
$$L(\varepsilon, T) = (1 - \varepsilon)\Delta H_{\text{f}}^{\text{metal}}, \tag{11}$$

provided that no chemical reactions or phase transformations occur between the solid phase and the surrounding gas atmosphere.



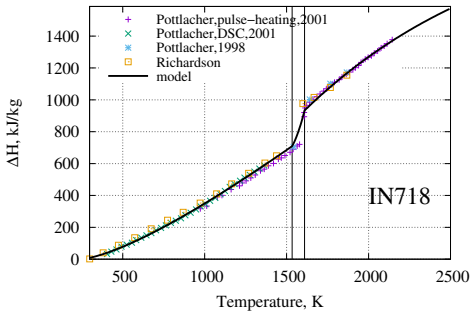

(a) SS316L

**References**
Mills (recommended values) [43], Pichler (subsecond ohmic pulse-heating apparatus) [68], and Wilthan (DSC, pulse-heating) [32].




(b) Ti–6Al–4V

**References**
Boivineau (resistive pulse heating devices at CEA Valduc and TU-Graz, DSC) [7], and Brooks (differential power-scanning calorimeter, differential temperature-scanning calorimeter, levitated-drop calorimeter) [62].




(c) Inconel 718

**References**
Hosaeus (DSC, 2001) [31], Pottlacher (1998) [70], and Richardson (DSC) [98].

**Figure 2**: Specific enthalpy of (a) SS316L, (b) Ti–6Al–4V, and (c) Inconel 718 alloys as functions of temperature $T$. The solidus $T_{\mathrm{sol}}$ and liquidus $T_m$ temperatures are designated by vertical lines.

**Table 5**: Polynomial expansion coefficients of specific enthalpy $\Delta H(T)$ (kJ kg$^{-1}$) for the selected temperature ranges.

| **Temperature range (K)** | $T^0$ | $T^{0.25}$ | $T^{0.5}$ | $T^1$ | $T^2$ | $T^3$ | $T^4$ | $T^5$ |
|---|---|---|---|---|---|---|---|---|
| *SS316L* | | | | | | | | |
| $T < 1679$ | $-4.23105 \times 10^2$ | 0 | 0 | 1.62843 | $-1.67136 \times 10^{-3}$ | $1.13421 \times 10^{-6}$ | $-2.79715 \times 10^{-10}$ | $1.98897 \times 10^{-15}$ |
| $1679 \leq T \leq 1713$ | $-1.27124 \times 10^4$ | 0 | 0 | 8.02941 | 0 | 0 | 0 | 0 |
| $T > 1713$ | $1.72076 \times 10^5$ | 0 | 0 | $3.78099 \times 10^2$ | $-3.29499 \times 10^{-1}$ | $1.43054 \times 10^{-4}$ | $-3.08764 \times 10^{-8}$ | $2.65082 \times 10^{-10}$ |
| *Ti–6Al–4V* | | | | | | | | |
| $T < 1878$ | $-4.63842 \times 10^1$ | 0 | 0 | 1.14177 | $-2.38101 \times 10^{-3}$ | $3.90051 \times 10^{-6}$ | $-2.36861 \times 10^{-9}$ | $4.75158 \times 10^{-13}$ |
| $1878 \leq T \leq 1921$ | $-1.20131 \times 10^4$ | 0 | 0 | 7.02070 | 0 | 0 | 0 | 0 |
| $T > 1921$ | -3911.47 | 94.9844 | 108.519 | 0 | 0 | 0 | 0 | 0 |
| *Inconel 718* | | | | | | | | |
| $T < 1533$ | 194.76 | 0 | -29.6649 | 1.09284 | 0 | 0 | 0 | 0 |
| $1533 \leq T \leq 1609$ | $3.39411 \times 10^4$ | 0 | 0 | $-4.51383 \times 10^1$ | $1.53034 \times 10^{-2}$ | 0 | 0 | 0 |
| $T > 1609$ | -4817.49 | 0 | 206.33 | -1.57021 | 0 | 0 | 0 | 0 |

### 3.3 Specific heat capacity $c_p$

The specific heat capacity of a powder mixture is typically calculated using a volume-weighted average and depends on temperature, gas density, and local porosity [24, 27]:

$$c_p^{\text{mixture}}(T) = \frac{c_p^{\text{metal}}(T)\rho^{\text{metal}}(1-\varepsilon) + c_p^{\text{gas}}\rho^{\text{gas}}\varepsilon}{\rho^{\text{metal}}(1-\varepsilon) + \rho^{\text{gas}}\varepsilon}, \tag{12}$$

where $c_p^{\text{metal}}(T)$ and $\rho^{\text{metal}}$ represent the specific heat capacity and density of the solid metal matrix, respectively, $T$ is the temperature, $c_p^{\text{gas}}$ and $\rho^{\text{gas}}$ are the corresponding values of the surrounding gas phase, and $\varepsilon$ is the local porosity.

The specific heat capacity of metallic alloys is one of the most complex thermodynamic characteristics regarding temperature dependence. Under constant-rate heating conditions, the measured $c_p$ of any complex alloy is defined by two primary factors: (i) its intrinsic specific heat, and (ii) extra thermal effects related to latent heat absorption or release during phase transformations, which introduce a significant contribution to the net balance of $c_p$. Numerous literature sources confirm that within the elevated temperature interval of $[0.7\,T_m \dots T_m]$, multicomponent alloys exhibit polymorphic transformations, magnetic phase transitions, and recrystallization phenomena. Pronounced sensitivity to the heating rate (thermal history) is also frequently observed. All aforementioned effects result in significant non-monotonicity, discontinuities, and abrupt leaps in the $c_p = f(T)$ curves. The thermophysical nature of these features is typically revealed through a thorough analysis of calorimetric DSC and DTA data in connection with the equilibrium phase diagram and intermetallic phase formation. Among the alloys studied in this work, Ti–6Al–4V and Inconel 718 both demonstrate such non-monotonic profiles due to the specific role of Ti and V in their chemical formulations.

According to experimental observations [7], the function $c_p(T)$ reveals a sharp jump around $T = 1200$ K, which directly reflects the $\alpha \to \beta$ allotropic transition in

the titanium lattice. The Ti–6Al–4V ternary alloy represents an $\alpha+\beta$ type solid solution with a distinct dominance of the $\alpha$-phase at room temperature. As temperature increases, the volume fraction of the $\beta$-phase grows, culminating in a full transition to the single-phase $\beta$ region at the transus temperature $T_\beta$, which highly depends on the exact chemical composition. Within this system, Al and V exert opposing thermodynamic effects. While Al acts as an active $\alpha$-phase stabilizer, shifting $T_\beta$ to higher temperatures, vanadium, conversely, stabilizes the $\beta$-phase and promotes a downward shift in $T_\beta$.

In the Inconel 718 superalloy, non-monotonic behavior of $c_p(T)$ is clearly observed within the intermediate temperature window between 940 and 1040 K. This anomaly is fundamentally linked [34] to microstructural transformations. Initially, the microstructure following high-temperature treatment at 1400 K and subsequent cooling comprises a $\gamma$ FCC solid solution matrix with finely dispersed particles of $\gamma'$ and $\gamma''$ localized predominantly at grain boundaries. These secondary phases exhibit a limited solvability that expands non-linearly with increasing temperature. At $T \sim 900$ K, these precipitate particles dissolve, providing a significant additional contribution to the total enthalpy $\Delta H$ and, consequently, inducing a substantial peak in the differential heat capacity $c_p = \partial\Delta H/\partial T$.

For the analytical approximation of the temperature dependence $c_p(T)$ of industrial alloys, the classic Maier–Kelley equation is often preferred [99]. However, the high-temperature region can be more effectively approximated by higher-order expansions [100]; the generalization of thermodynamic function expansions in regions containing phase singularities can be elegantly implemented in the form of a Laurent series:

$$c_p(T) = a_{-4}T^{-4}+a_{-3}T^{-3}+a_{-2}T^{-2}+a_{-1}T^{-1}+a_0+a_1T+a_2T^2+a_3T^3+a_4T^4. \quad (13)$$

The specific heat capacity over a wide temperature interval is controlled by several distinct physical mechanisms, each characterized by its own temperature sensitivity. At high temperatures well above the Debye temperature, $c_p$ asymptotes toward the classical limit predicted by the Dulong–Petit law [100]. At intermediate temperatures, however, lattice anharmonicity introduces terms of higher positive powers into the expansion. For metals and alloys, the electronic contribution to $c_p$ scales linearly with $T$ according to the Sommerfeld free-electron theory, which yields the $a_1T$ term. At temperatures approaching the solidus, the equilibrium concentration of vacancies increases exponentially, causing the appearance of the $T^{-1}$ and $T^{-2}$ negative power terms. Consequently, a proper description of phase transitions requires mathematical models containing both positive and negative powers.

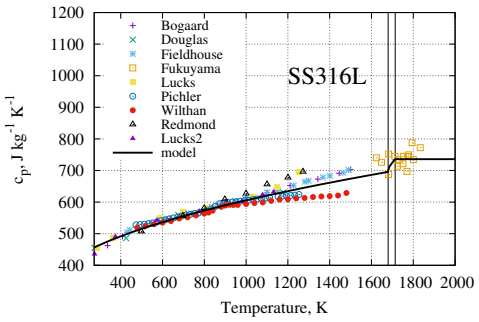
An approach rooted in the thermodynamics of metallurgical processes is systematically utilized by Kenneth C. Mills [101] via an extended variant of the Maier–Kelley equation:

$$c_p(T) = a + bT + cT^2 + dT^{-1} + eT^{-2}. \tag{14}$$

The same mathematical expansion is applied in foundational thermodynamic databases compiled by Kubaschewski [102] and Barin [103]. Similarly, the Scientific Group Thermodata Europe (SGTE) [104] recommends modeling the property via the expression:

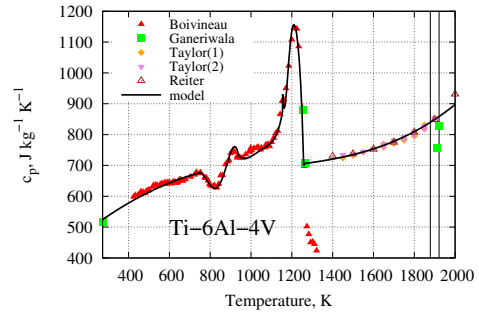
$$c_p(T) = a + bT + cT^2 + dT^3 + eT^{-1} + fT^{-2}. \tag{15}$$

In the present study, we have expanded the polynomial powers up to $T^{-4} \dots T^4$ since this symmetric Laurent formulation ensures superior fitting accuracy near phase transformation singularities. Specifically, high powers provide an excellent description of structural asymmetry and capacity leaps while strictly preserving functional continuity. The resulting $c_p(T)$ curves evaluated for all three alloys are illustrated in Fig. 3, and the corresponding piecewise expansion coefficients are compiled in Table 6.



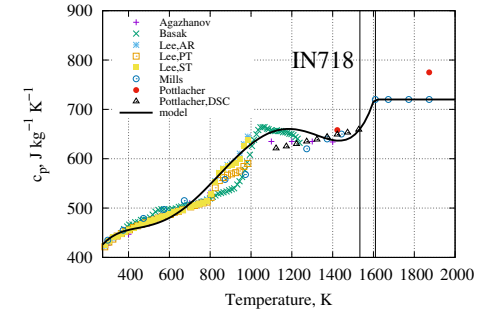

(a) SS316L

**References**
Bogaard (review and data compilation) [59], Douglas (precision Bunsen ice calorimeter with drop method) [105, 106], Fieldhouse [89], Fukuyama (laser-modulation calorimetry) [65], Lucks [107, 108], Pichler (commercial Netzsch DSC 404 C Pegasus) [68], Wilthan (Netzsch DSC 404 and pulse-heating data) [32], and Redmond [109].




(b) Ti–6Al–4V

**References**
Basak (millisecond-resolution pulse-heating system) [34], Boivineau (TU-Graz system, DSC and pulse-heating) [7], Ganeriwala (modeling via multiphysics code Diablo) [94], Taylor (high-speed pyrometer transient technique) [110], and Reiter (millisecond and microsecond pulse-heating techniques) [35].




(c) Inconel 718

**References**
Agazhanov (laser flash, dilatometric method, and DSC) [29], Basak (NIST millisecond-resolution pulse-heating system) [34], Lee (DSC analysis for as-received, precipitation-treated, and solution-treated samples) [30], Mills (recommended dataset) [58], and Pottlacher (fast resistive pulse heating technique and DSC) [33, 70].

**Figure 3**: Calculated specific heat capacity of (a) SS316L steel, (b) Ti–6Al–4V alloy, and (c) Inconel 718 as functions of temperature $T$. The vertical lines indicate the solidus $T_{\mathrm{sol}}$ and liquidus $T_m$ temperatures.

**Table 6**: Laurent series and polynomial expansion coefficients derived for the specific heat capacity $c_p(T)$ (J kg$^{-1}$ K$^{-1}$) of SS316L, Ti–6Al–4V, and Inconel 718 alloys for given temperature ranges.

| **Temperature range (K)** | $T^{-2}$ / $T^0$ | $T^{-1}$ / $T^1$ | $T^0$ / $T^2$ | $T^1$ / $T^3$ | $T^2$ / $T^4$ | $T^3$ / $T^5$ |
|---|---|---|---|---|---|---|
| *SS316L (Maier–Kelley / Laurent powers: $T^{-2}$ to $T^3$)* | | | | | | |
| $298 - 1679$ | 0 | 0 | $2.101 \times 10^2$ | 0 | 0 | $1.048 \times 10^{-7}$ |
| $1679 - 1713$ | 0 | 0 | $-8.116 \times 10^2$ | $9.040 \times 10^{-1}$ | 0 | 0 |
| $1713 - 3000$ | 0 | 0 | $7.360 \times 10^2$ | 0 | 0 | 0 |
| *Ti–6Al–4V (High-order polynomial powers: $T^0$ to $T^5$)* | | | | | | |
| $298.15 - 750.837$ | $3.7828569 \times 10^0$ | $6.1516805 \times 10^{-1}$ | $-2.8993917 \times 10^{-4}$ | 0 | 0 | 0 |
| $750.837 - 939.515$ | $1.1258219 \times 10^5$ | $-1.6313212 \times 10^3$ | $6.2754916 \times 10^0$ | $-1.0404929 \times 10^{-2}$ | $7.9757701 \times 10^{-6}$ | $-2.3277462 \times 10^{-9}$ |
| $939.515 - 1155.04$ | $-1.4303552 \times 10^6$ | $7.3586097 \times 10^3$ | $-1.5065242 \times 10^1$ | $1.5356917 \times 10^{-2}$ | $-7.7974868 \times 10^{-6}$ | $1.5782864 \times 10^{-9}$ |
| $1155.04 - 1258.59$ | $1.8070973 \times 10^9$ | $-7.4483021 \times 10^6$ | $1.2278417 \times 10^4$ | $-1.0119354 \times 10^1$ | $4.1696036 \times 10^{-3}$ | $-6.8717079 \times 10^{-7}$ |
| $1258.59 - 3000$ | $3.3770361 \times 10^0$ | $8.0553049 \times 10^{-1}$ | $-6.5345471 \times 10^{-4}$ | $1.9532729 \times 10^{-7}$ | 0 | 0 |
| *Inconel 718 (High-order polynomial powers: $T^0$ to $T^5$)* | | | | | | |
| $298 - 1609$ | $-7.849 \times 10^1$ | 4.123 | $-1.225 \times 10^{-2}$ | $1.712 \times 10^{-5}$ | $-1.074 \times 10^{-8}$ | $2.467 \times 10^{-12}$ |
| $1609 - 3000$ | $7.200 \times 10^2$ | 0 | 0 | 0 | 0 | 0 |

## 3.4 Thermal conductivity $k$

Thermal conductivity $k$ (W m$^{-1}$ K$^{-1}$) in metal powders during PBF-LB and PBF-G (Powder Bed Fusion using G-code) processing is fundamentally defined by the conductivities $k^{\mathrm{m}}$ of the solid or melted metal matrix and $k^{\mathrm{gas}}$ of the surrounding gas phase, respectively. For a proper transport analysis, the temperature and pressure dependencies of $k^{\mathrm{gas}}(T, P)$ and $k^{\mathrm{m}}(T)$ are first introduced. Subsequently, these functions are employed as inputs for advanced models of heat transport in powder beds that explicitly account for the local porosity $\varepsilon$ of the material [27].

### 3.4.1 Heat transfer in the gas atmosphere and metals

**Table 7**: Coefficients of the gas thermal conductivity $k^{\mathrm{gas}} = f(T, P)$ from Eq. (16), provided for vacuum, air, nitrogen, and argon atmospheres.

| **Gas phase** | $T_0$ (K) | $k(T_0)$ (W m$^{-1}$ K$^{-1}$) | $x$ | $B$ |
|---|---|---|---|---|
| Vacuum | 1 | 0 | 1 | 1 |
| Air | 300 | $26.3 \times 10^{-3}$ | 0.9 | 5.85 |
| $N_2$ | 273 | $24.3 \times 10^{-3}$ | 0.8 | 5.95 |
| Ar | 373 | $25.6 \times 10^{-3}$ | 0.5 | 5 |

The temperature and pressure dependence of $k^{\mathrm{gas}}(T, P)$ follows from the non-linear interpolation of experimental data [85]:

$$k^{\mathrm{gas}}(T, P) = k(T_0) \left( \frac{T}{T_0} \right)^{x} \frac{\log_{10} P}{B}, \tag{16}$$

where $k(T_0)$, $T_0$, $x$, and $B$ represent the empirical fitting coefficients summarized in Table 7. For thermodynamic reasons common to both specific heat and thermal conductivity described in Sec. 3.3, the thermal conductivity $k^{\mathrm{m}}$ of industrial alloys also

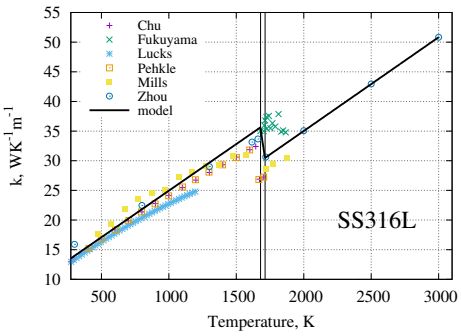
exhibits a highly non-linear temperature dependence. Thus, the computational optimization approach discussed in Sec. 3.3 has been implemented to approximate the temperature dependence of the metal conductivity, expressed as $k_{\text{metal}} = f(T)$. Table 8 gathers the piecewise polynomial expansion coefficients for all investigated alloys, while Fig. 4 summarizes the compiled experimental datasets alongside the resulting theoretical curves of $k^{\text{m}}(T)$.

**Table 8**: Polynomial expansion coefficients of the bulk thermal conductivity $k^{\text{m}}(T)$ (W m$^{-1}$ K$^{-1}$) of SS316L, Ti–6Al–4V, and Inconel 718 for the selected temperature ranges.

| **Temperature range (K)** | $T^0$ | $T^1$ | $T^{0.2}$ | $T^{0.6}$ |
|---|---|---|---|---|
| *SS316L* | | | | |
| 298 – 1679 | 9.248 | $1.571 \times 10^{-2}$ | 0 | 0 |
| 1679 – 1713 | $2.98386 \times 10^{2}$ | $-1.56499 \times 10^{-1}$ | 0 | 0 |
| 1713 – 3000 | 3.38621 | $1.58145 \times 10^{-2}$ | 0 | 0 |
| *Ti–6Al–4V* | | | | |
| 298 – 1878 | 1.67846 | $1.30835 \times 10^{-2}$ | 0 | 0 |
| 1878 – 1921 | −71.801 | $5.22099 \times 10^{-2}$ | 0 | 0 |
| 1921 – 3000 | −6.66 | $1.83 \times 10^{-2}$ | 0 | 0 |
| *Inconel 718* | | | | |
| 298 – 3500 | −1.60683 | 0 | 1.36774 | 0.287506 |

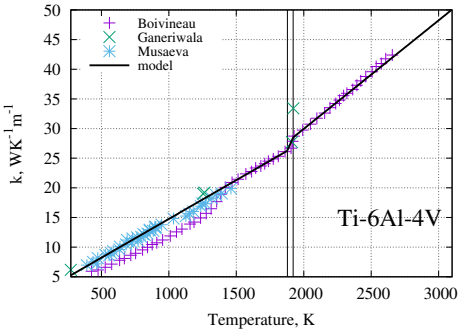
## 3.5 Heat transfer in powders

After evaluating various analytical models for dry and partially melted powders proposed by Lykov, Ofuchi–Kunii–Smith, Zehnder–Schlünder, Chen–Cheng–Hsu, Kaviany, and Hadley [23, 24, 26, 28, 73, 119, 120], this research has been narrowed to the highly adaptable Hadley statistical model suggested in [73]. The model introduces a consolidation coefficient $\alpha_H$, which effectively behaves as a crossover parameter matching two limiting cases: the Maxwell upper bound (Lykov model [119]) and the lower



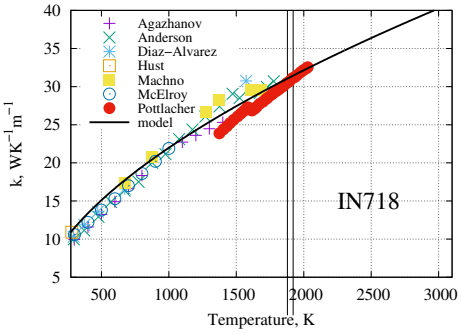

(a) SS316L

**References**
Chu (data compilation) [111], Fukuyama (laser-modulation calorimetry) [65], Lucks [107], Pehlke (thermophysical database) [67], Mills (recommended dataset) [56], and Zhou (finite element simulation) [112].




(b) Ti–6Al–4V

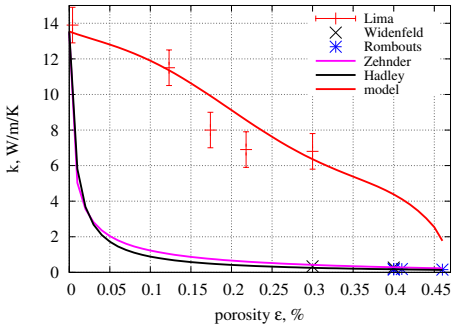
**References**
Boivineau (TU-Graz system, DSC and pulse-heating) [7], Ganeriwala (multiphysics modeling via Diablo code) [113], and Musaeva (calorimetry and steady-state heat flow methods) [114].




(c) Inconel 718

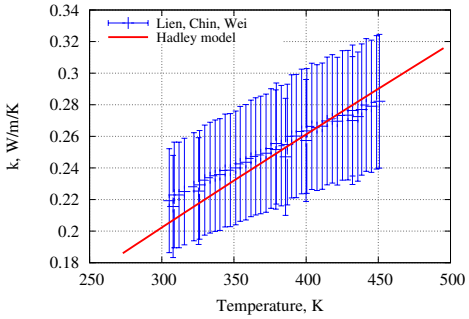
**References**
Agazhanov (laser flash, dilatometry, and DSC) [29], Anderson (laser-assisted machining analysis) [115], Hust (axial one-dimensional heat flow method) [116], Machno [117], McElroy (guarded longitudinal heat flow technique) [118], and Pottlacher (fast resistive pulse heating technique) [33].

**Figure 4**: Thermal conductivity of bulk $k^{\mathrm{m}}$ matrix for (a) SS316L, (b) Ti–6Al–4V alloy, and (c) Inconel 718. The solidus $T_{\mathrm{sol}}$ and liquidus $T_m$ temperatures are designated by vertical lines.




(a) SS316L, $k_{\text{eff}}(\varepsilon, T)$ at $T = 273$ K

**References**
Lima (photoacoustic and thermal relaxation methods for partially compacted powders under mechanical pressure) [11], Widenfeld (steady-state conditions) [9], and Rombouts (photopyroelectric measurements) [10].



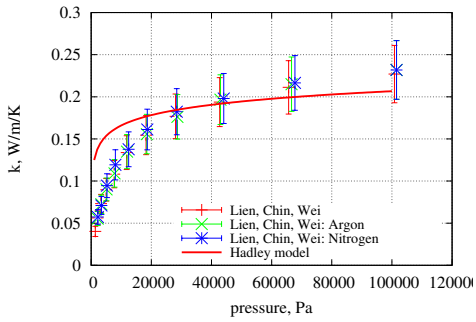

(b) SS316L, $k_{\text{eff}}(\varepsilon, T)$ at $\varepsilon = 0.38$

**References**
Lien, Chin, and Wei (transient hot-wire method) [8].

**Figure 5**: Effective thermal conductivity $k_{\text{eff}}(\varepsilon, T)$ of the SS316L powder: (a) comparison of the present model (Hadley), Eq. (17) with $\alpha_H = 8 \times 10^{-3}$, our model in the dry powder limit with $\alpha_H = 0.01$, and the Zehnder–Schlünder model [26] for dry powders as a function of the local porosity $\varepsilon$; (b) literature data and models for the effective thermal conductivity $k_{\text{eff}}(\varepsilon, T)$ as a function of temperature $T$ at a fixed porosity of $\varepsilon = 0.38$.

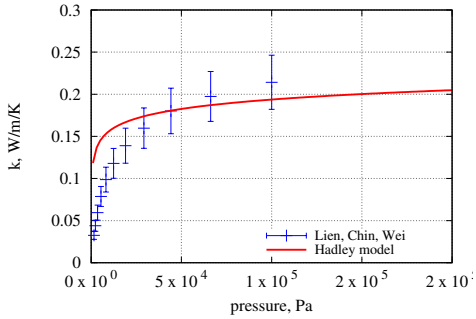
bound model [24]. Utilizing this approach, it is possible to cover most scenarios of partial melting and track consolidation of metallic powders during laser processing and consolidation [27]:

$$k_{\text{eff}} = k^{\text{gas}}(1-\alpha_H)\frac{\varepsilon f_0 + (1-\varepsilon f_0)\left[k^{\text{metal}}/k^{\text{gas}}\right]}{1-\varepsilon(1-f_0)+\varepsilon(1-f_0)\left[k^{\text{metal}}/k^{\text{gas}}\right]} + k^{\text{gas}}\alpha_H \frac{2(1-\varepsilon)\left[k^{\text{metal}}/k^{\text{gas}}\right]^2 + (1+2\varepsilon)\left[k^{\text{metal}}/k^{\text{gas}}\right]}{1-\varepsilon+(2+\varepsilon)\left[k^{\text{metal}}/k^{\text{gas}}\right]}, \quad (17)$$




(a) SS316L, $k_{\text{eff}}(P)$

**References**
Lien, Chin, and Wei (transient hot-wire method) [8].




(b) Ti–6Al–4V, $k_{\text{eff}}(P)$

**References**
Lien, Chin, and Wei (transient hot-wire method) [8].

**Figure 6**: Verification of the effective thermal conductivity $k_{\text{eff}}(P)$ in metal powders as a function of gas pressure $P$ by comparing the modified Hadley model with experimental data from [8] at a fixed porosity of $\varepsilon = 0.38$ and a temperature of $T = 273$ K: (a) SS316L and (b) Ti–6Al–4V.

where $f_0$ is an empirical constant determined as $f_0 = 0.9$ in our previous study [27]. This model, defined by Eq. (17), provides a proper description of both partially melted and dry (i.e., unprocessed) powders within a single coherent approach. At $\alpha_H \simeq 0.01$, the medium is loosely packed and $k_{\text{eff}}$ closely matches the data reported by Nozad et al. [121, 122] for dry powders. Using our internal experimental data, we obtained $\alpha_H = 8 \times 10^{-3}$ for the dry steel powder. This approximation can be reliably extended to other metallic alloys as a first estimate.

Following the numerical procedure introduced in our previous work [27], the Hadley model has been successfully applied to partially melted powder beds. Based on the assumption of a close-to-spherical particle morphology and following averaging over random particle packings within the representative volume element during consolidation, it is possible to eliminate the explicit dependence on the particle diameter $d_C$, which commonly complicates alternative formulations [123, 124]. Therefore, a new analytical formula for the consolidation coefficient $\alpha_H$ is proposed in the form:

$$\alpha_H = \sqrt[3]{1 - \frac{\varepsilon}{\varepsilon_0}}, \tag{18}$$

where $\varepsilon_0$ represents the initial porosity of the unprocessed powder bed. The functional relation for $\alpha_H$ expressed in Eq. (18) demonstrates an excellent agreement with experimental data and multi-physics numerical simulations of partially melted compacts [27]. Figs. 5 and 6 illustrate the resulting effective thermal conductivity profiles of SS316L and Ti–6Al–4V powders as functions of local porosity, temperature, and atmospheric gas pressure.

## 3.6 Electrical resistivity $\rho_{\mathrm{el}}$

Electrical resistivity $\rho_{\mathrm{el}}$ ($\Omega\,\mathrm{m}$) is a fundamental transport measure of a material's resistance to electric current. It is defined as the reciprocal of electrical conductivity, $\rho_{\mathrm{el}} = 1/\sigma_{\mathrm{el}}$, and uniquely characterizes the conductor matrix. Electrical conductivity is directly related to thermal conductivity $k$ by the Wiedemann–Franz law:

$$\frac{k}{\sigma_{\mathrm{el}}} = k\rho_{\mathrm{el}} = \frac{\pi^2}{3}\left(\frac{k_{\mathrm{B}}}{e}\right)^2 T, \tag{19}$$

where $k_{\mathrm{B}}$ is the Boltzmann constant, $e$ represents the elementary charge, and $T$ is the absolute temperature. This thermodynamic law remains valid in both low- and high-temperature boundaries where the approximation of electronic relaxation time applies.

For metals and industrial alloys, the temperature dependence of $\rho_{\mathrm{el}}$ is governed by several concurrent electron scattering mechanisms. According to Matthiessen's rule, the total electrical resistivity can be formulated as the sum:

$$\rho_{\mathrm{el}}(T) = \rho_0 + \rho_{\mathrm{ph}}(T) + \rho_{\mathrm{d}}(T) + \rho_{\mathrm{m}}(T), \tag{20}$$

where $\rho_0$ is the residual resistivity resulting from electron scattering off crystal lattice defects (assumed to be temperature-independent), $\rho_{\mathrm{ph}}(T)$ represents the phonon contribution driven by scattering from thermal lattice vibrations, $\rho_{\mathrm{d}}(T)$ is the contribution from scattering on structural defects and chemical impurities, and $\rho_{\mathrm{m}}(T)$ is the quantum contribution associated with localized magnetic interactions. The net electrical resistivity of metallic alloys displays a complex relationship with temperature, influenced by multiple processing and structural factors:

1. Electron-phonon scattering dominates at elevated temperatures, yielding a strictly linear contribution $\rho_{\mathrm{ph}}(T) \propto T$ above the characteristic Debye temperature.

2. Lattice vibration anharmonicity introduces higher-order polynomial terms at intermediate temperature intervals.
3. Structural phase transformations, such as the polymorphic $\alpha + \beta \rightarrow \beta$ allotropic transition in Ti–6Al–4V or the dissolution of secondary $\gamma'$ and $\gamma''$ precipitate phases in Inconel 718, induce distinct anomalies, including local extrema and sharp slope variations.
4. Pronounced sensitivity to thermal history and processing heating rates is observed, particularly for Ti–6Al–4V, where the transus temperature shifts significantly under microsecond pulse-heating conditions compared to quasi-static states [7, 33, 34, 118].

As established in the heat capacity analysis (Sec. 3.3), the most robust approach for approximating thermophysical properties across extended temperature ranges containing phase transitions is a piecewise continuous polynomial representation utilizing Laurent expansions with both positive and negative powers of temperature. This optimization approach, inspired by the work of Mills [101] and the international SGTE group [104], is equally applied here to model the electrical resistivity $\rho_{\mathrm{el}}(T)$.

To measure the electrical resistivity of SS316L, Ti–6Al–4V, and Inconel 718, various high-temperature experimental techniques are employed. These include fast ohmic pulse-heating, with independent evaluation of the initial geometry $\rho_{\mathrm{IG}}$ and thermal expansion corrected $\rho_{\mathrm{corr}}$ profiles [7, 33, 68], millisecond pulse-calorimetry [34, 35], the standard four-probe stationary method for baseline calibration at room temperature [125], and the comparative guarded longitudinal heat flow technique for low-temperature validation [116, 118]. A critical feature common to all transient pulse-heating frameworks is that neglecting the thermal expansion correction results in a severe 5–10% underestimation of $\rho_{\mathrm{el}}(T)$ in the liquid state. This error critically propagates into subsequent indirect evaluations of thermal conductivity via the Wiedemann–Franz relation [7, 32, 68].

For the SS316L alloy, which undergoes no solid-state polymorphic transformations, the temperature dependence of $\rho_{\mathrm{el}}(T)$ in the solid region is accurately captured by a second-degree polynomial:

$$\rho_{\mathrm{el}}(T) = a + bT + cT^2, \quad \text{for} \quad 500\,\mathrm{K} < T < 1679\,\mathrm{K}. \tag{21}$$

Within the melting range ($1679 \leq T \leq 1713\,\mathrm{K}$), a standard linear interpolation is implemented. In the single-phase liquid region above the liquidus, the resistivity corrected for thermal expansion increases monotonically with temperature [68] according to:

$$\rho_{\mathrm{el}}(T) = a + bT, \quad \text{for} \quad T > 1713\,\mathrm{K}, \tag{22}$$

where the expansion coefficient $b$ is strictly positive and approximately equal to $1.9 \times 10^{-4}\,\mu\Omega\,\mathrm{m\,K^{-1}}$.

The Ti–6Al–4V alloy exhibits highly complex transport behavior due to the polymorphic $\alpha + \beta \rightarrow \beta$ transformation. In the low-temperature $\alpha + \beta$ phase field below 1150 K, $\rho_{\mathrm{el}}(T)$ grows monotonically and can be effectively fit by standard linear or quadratic functions [125]. The transformation interval between 1150 and 1350 K represents the most critical region. Driven by the kinetics of the $\alpha + \beta \rightarrow \beta$ transition, $\rho_{\mathrm{el}}(T)$ exhibits a heavily non-monotonic profile, reaching a local maximum near 900 K, followed by a sharp drop to a local minimum near 1250–1300 K, before rising again in the single-phase $\beta$ region [7, 125]. This anomalous path cannot be replicated by a single low-degree polynomial. Instead, it requires either dedicated piecewise continuous fits for each discrete phase window or a high-order Laurent series to smoothly capture the local extrema. In the single-phase $\beta$ zone ($T > 1350\,\mathrm{K}$) and the subsequent liquid phase, the corrected resistivity $\rho_{\mathrm{el}}(T)$ follows a linear dependence with a positive slope. A key transport feature of Ti–6Al–4V is its behavior during the solid-liquid transition: the uncorrected raw resistivity $\rho_{\mathrm{el0}}(T)$ shows a non-physical drop upon

melting ($\Delta\rho_{\mathrm{el0}} < 0$). This artifact completely disappears once the volumetric thermal expansion correction is integrated, correctly yielding a positive resistivity jump, $\Delta\rho_{\mathrm{el}} > 0$ [7].

With the Inconel 718 superalloy, $\rho_{\mathrm{el}}(T)$ exhibits a complex sequence of structural phase transformations. In the low-temperature range (300–800 K), $\rho_{\mathrm{el}}(T)$ increases monotonically with temperature. A highly complex transport behavior is observed within the intermediate window between 800 and 1000 K, where $\rho_{\mathrm{el}}(T)$ reaches a local maximum near 900 K and subsequently decreases to a local minimum near 1000 K [118]. This distinct anomaly is fundamentally attributed to the dissolution kinetics of the key strengthening phases, namely $\gamma'$ ($Ni_3$(Al,Ti)) and $\gamma''$ ($Ni_3$Nb) [34]. Consequently, a simple linear or quadratic fit is insufficient for this region, and a higher-order polynomial (fourth degree) is required to accurately capture the local maximum and minimum.

Above 1000 K, following the completion of these microstructural phase transformations, $\rho_{\mathrm{el}}(T)$ increases linearly with temperature up to the solidus limit [33]. Pottlacher et al. [33] provided an explicit polynomial fit for both uncorrected and expansion-corrected profiles. In the single-phase solid region ($1000 < T < 1528\,\mathrm{K}$), the electrical resistivity corrected for volumetric thermal expansion is described by a third-degree polynomial:

$$\textbf{Inconel 718}\text{: } \rho_{\mathrm{el}}(T) = -0.960 + 0.005T - 3.919\times10^{-6}T^2 + 9.713\times10^{-10}T^3, \quad \text{for} \quad 1000\,\mathrm{K} < T < 1528\,\mathrm{K}. \tag{23}$$

In the liquid phase ($1610 < T < 2100\,\mathrm{K}$), the corrected resistivity follows a stable linear dependence:

$$\textbf{Inconel 718}\text{: } \rho_{\mathrm{el}}(T) = 1.251 + 1.364\times10^{-4}T, \quad \text{for} \quad 1610\,\mathrm{K} < T < 2100\,\mathrm{K}. \tag{24}$$

The uncorrected raw resistivity $\rho_{\mathrm{el0}}(T)$ exhibits a maximum near 1200 K followed by a continuous decrease, which acts as a geometric artifact of the transient calculation. For the liquid phase without the volumetric expansion correction, a linear fit with a significantly smaller slope must be implemented:

$$\textbf{Inconel 718}\text{: } \rho_{\mathrm{el0}}(T) = 1.307 + 3.438 \times 10^{-5} T, \quad \text{for} \quad 1610\,\mathrm{K} < T < 2100\,\mathrm{K}. \quad (25)$$

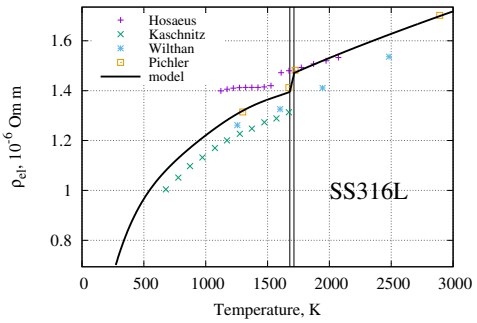
It should also be noted that $\rho_{\mathrm{el}}(T)$ of Inconel 718 is highly sensitive to the prior thermal history and heat treatment conditions, which can introduce localized variations of up to $\pm 1.5\%$ over time at temperatures within the range of 600–900 K [118]. Therefore, Inconel 718 is not recommended as a standard reference material for high-precision calibration measurements unless its baseline thermal history is exceptionally well established [126].

Based on the thorough analysis of experimental datasets compiled from the literature, the following general polynomial expansion strategies are recommended for approximating the temperature dependence $\rho_{\mathrm{el}} = f(T)$:

- **SS316L:** A standard quadratic expansion in the solid phase, transitioning to a strict linear function in the single-phase liquid region.
- **Ti–6Al–4V:** A linear or quadratic fit within the low-temperature $\alpha + \beta$ field; dedicated separate linear functions or a higher-order Laurent series for the allotropic transformation interval to properly isolate the local maximum and minimum; and a positive-slope linear function in the single-phase $\beta$ region and liquid state following volumetric expansion correction.
- **Inconel 718:** A higher-order polynomial (minimum fourth degree) in the solid state to accurately isolate the localized maximum near 900 K and the minimum near 1000 K, transitioning to a stable linear fit in the liquid phase for both corrected and uncorrected configurations.

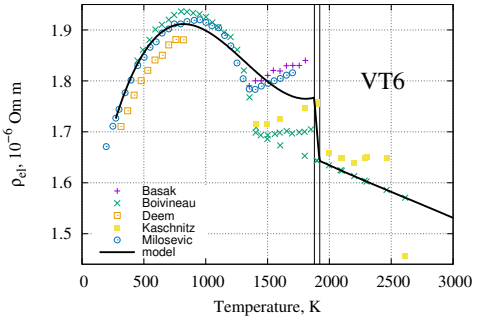
**Table 9**: Piecewise polynomial expansion coefficients derived for the electrical resistivity $\rho_{\mathrm{el}}(T)$ ($\mu\Omega\,\mathrm{m}$) of SS316L, Ti–6Al–4V, and Inconel 718 alloys for given temperature ranges.

| **Temperature range (K)** | $T^0$ | $T^1$ | $T^2$ | $T^3$ | $T^4$ | $T^5$ |
|---|---|---|---|---|---|---|
| *SS316L* | | | | | | |
| $298-1679$ | $-0.0461101$ | $4.14023\times10^{-3}$ | $-6.54767\times10^{-6}$ | $5.81120\times10^{-9}$ | $-2.58613\times10^{-12}$ | $4.49240\times10^{-16}$ |
| $1679-1713$ | $-2.06276$ | $2.05882\times10^{-3}$ | 0 | 0 | 0 | 0 |
| $1713-3000$ | 0.740303 | 0 | 0 | $5.43411\times10^{-13}$ | 0 | 0 |
| *Ti–6Al–4V* | | | | | | |
| $273-1878$ | 1.43923 | $1.35640\times10^{-3}$ | $-1.20147\times10^{-6}$ | $3.04690\times10^{-10}$ | 0 | 0 |
| $1878-1921$ | 7.23444 | $-2.91054\times10^{-3}$ | 0 | 0 | 0 | 0 |
| $1921-3550$ | 1.96871 | $-2.55261\times10^{-4}$ | $5.91686\times10^{-8}$ | $-7.56988\times10^{-12}$ | 0 | 0 |
| *Inconel 718* | | | | | | |
| $298-1533$ | 1.08529 | $-4.46749\times10^{-3}$ | $5.17135\times10^{-4}$ | $-3.08833\times10^{-9}$ | 0 | 0 |
| $1533-1609$ | 0.110681 | $1.21607\times10^{-2}$ | $5.42825\times10^{-4}$ | 0 | 0 | 0 |
| $1609-3000$ | 1.26202 | $-1.63701\times10^{-4}$ | $1.34385\times10^{-4}$ | 0 | 0 | 0 |



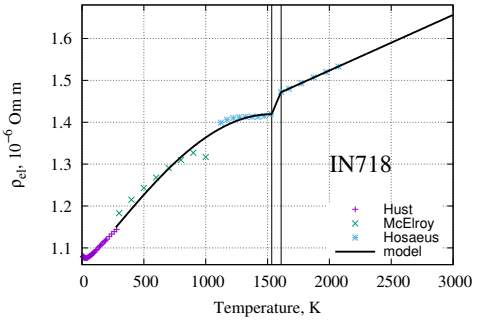

(a) SS316L

**References**
Pichler (subsecond ohmic pulse-heating apparatus) [68], Kaschnitz (millisecond pulse-heating) [127], and Wilthan (DSC, pulse-heating) [32].




(b) Ti–6Al–4V

**References**
Basak (millisecond-resolution pulse-heating system) [34], Boivineau (TU-Graz system, DSC and pulse-heating) [7], Cezairliyan (transient subsecond technique) [110], Deem [128], Kaschnitz (millisecond and microsecond pulse-heating) [35], and Milošević (subsecond pulse calorimetry) [125].




(c) Inconel 718

**References**
Pottlacher (fast resistive pulse heating technique) [33], Hust (axial one-dimensional heat flow method) [116], and McElroy (guarded comparative longitudinal heat flow technique) [118].

**Figure 7**: Electrical resistivity of (a) SS316L steel, (b) Ti–6Al–4V alloy, and (c) Inconel 718 as functions of temperature $T$. The vertical lines indicate the liquidus and solidus temperatures.

## 3.7 Surface tension

The surface tension coefficient $\gamma$ of metal melts describes a specific contractive force acting on the surface between the liquid and gas phases. The liquid surface is stimulated to reduce its surface area, thereby lowering the overall free energy of the multiphase system. The physical reason for surface tension is a difference in the balance of intermolecular forces between molecules in the bulk and on the surface. The surface molecules have fewer neighbors, thus the net force appears directed inwards of the liquid phase.

The surface tension for pure liquid metals decreases with increasing temperature $T$, hence $d\gamma/dT < 0$. It happens because heating increases the kinetic energy of atoms at the liquid-vapour interface. That weakens their interatomic interactions. Alloying can also strongly affect the surface tension [65, 69, 129, 130]. For example, the addition of certain alloying elements can either increase or decrease the surface tension. Some metals are prone to oxidation and formation of surface oxide films, which may either alter the surface tension during metal processing. Thus, correct assessment of the $\gamma = f(T)$ function for a specific alloy is a complicated task that should account for the following methodological complexities.

*(i) Large scatter and poor reproducibility of experimental data.* In experimental studies on SS316L, a significant scatter in the experimentally measured values of surface tension is usually observed. Therefore, the chosen approximation of measured data significantly affects both the values of $\gamma$ itself and the thermal coefficient of surface tension $d\gamma/dT$. As a result, the study [131] shows that different linear approximations of surface tension lead to distinctive convection patterns in the simulation of melt pool hydrodynamics. Thus, melt pools with varying geometrical parameters are predicted.

*(ii) Effect of the chemical composition, oxygen level, and sulfur content.* The most reasonable explanation for this scatter is the presence of sulfur and oxygen impurities in the tested experimental samples. The studies on molten pool formation during

welding [132–134] have shown that if the sulfur concentration in stainless steels exceeds a specific threshold, then the thermo-capillary shear stress changes its sign. The sulfur concentration range between 30 and 60 ppm is identified as the threshold beyond which the Marangoni-driven flow reverses its direction [132, 135, 136]. As confirmation, in [137] it is shown that the surface tension of SS316L yields $d\gamma/dT > 0$ within a certain temperature range because of the relatively high content of sulfur (40 ppm) and oxygen (500 ppm). The underlying reason is the presence of surface-active elements with concentrations exceeding the abovementioned thresholds. Thus, oxides and sulfides in the melt pool not only change the magnitude of $d\gamma/dT$ but also reverses its sign [138–140]. More data on this effect is provided in [138–140]. As a precondition for all alloys analyzed in this paper, the function $\gamma(T)$ is considered as experiment-dependent and not uniquely defined for the specific material. The surface tension coefficient exhibits high sensitivity to the sulfur and oxygen concentrations, even at the level of a few tens of ppm.

*(iii) Effect on hydrodynamics in the molten pool.* In additive manufacturing, the flow pattern and fluid velocity intensity are mainly controlled by Marangoni convection. The temperature gradient along the melt pool surface is as high as $dT/d\vec{\tau} \sim 10^7$ K m$^{-1}$, where $\vec{\tau}$ is the vector tangential to the pool surface. Hence, the sign and magnitude of $d\gamma/dT$ determine the flow direction and its intensity in the melt pool [141]. The Marangoni effect on the surface of the molten pool directs the liquid from the region of low surface tension to the one of high surface tension. For most metals and alloys, $d\gamma/dT < 0$ and it leads to outward convection in the molten pool, i.e. the flow is directed from the high to low temperature regions. If $d\gamma/dT < 0$, the flow is oppositely directed and inward from the pool edge to its center.

*(iv) Non-monotonic temperature dependence near the boiling temperature.* Surface tension deviates from the linear dependence on temperature if the melt is significantly overheated above the melting temperature. The latest experimental and simulation

results on steels [142] show that the surface tension takes lower values than expected theoretically if the temperature both exceeds $T_m$ and is shifted to the boiling temperature $T_{boil.}$. It means that the reduction of force interaction between atoms has a more prominent effect than was suggested in the literature before. Once the melt temperature approaches its boiling point $T_{boil}$, the surface tension does not vanish completely, and it varies between 15% and 25% of its value $\gamma(T = T_m)$ measured at the melting temperature. This observation is explained by the fact that at $T = T_{boil}$ the melt is still far from the state of super-critical fluids where the difference between the liquid and vapor disappears.

## Derived expressions and employed approximations.

The temperature dependence of the surface tension coefficient is generally expressed by a linear function of temperature [143]:

$$\gamma(T)_{\text{general}} = \gamma(T_m) + \frac{d\gamma}{dT}(T - T_m), \tag{26}$$

where $\gamma(T_m)$ is the surface tension coefficient at the melting temperature $T_m$ and $d\gamma/dT$ is its thermal coefficient. The thermal coefficient is usually of the order of $d\gamma/dT \sim 10^{-4}$ N m$^{-1}$ K$^{-1}$. If this coefficient is unknown, this value is recommended as a first-choice estimate for various alloys.

Usually, the $\gamma(T)$ approximation depends on the particular chemical composition and temperature range. The linear, $2^{nd}$ and $3^{rd}$ order polynomial, and nonlinear thermodynamically consistent models [144, 145] are invoked for this purpose. In the present work, the literature data were approximated with a function linear in $T$. For numerical simulation, the focus is laid on the value of $\gamma(T_m)$ and the sign of $d\gamma/dT$. The approximated results are summarized in Table 10 where the proper coefficients for all

studied alloys are listed. The corresponding plots are depicted in Figure 8. The provided approximations are valid in the vicinity of the melting temperature and up to 300 K above $T_m$.

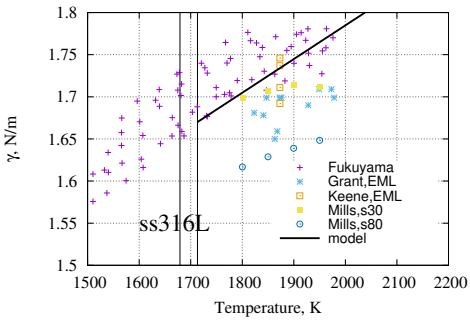
The experimental data on SS316L clearly show that the surface tension of liquid alloys undercooled below the melting temperature still complies with the linear law given by Eq. 26. This conclusion has been confirmed [41, 42] by many qualified research groups through levitation measurements of surface oscillations of molten metallic droplets. Upon solidification, the surface tension changes to the surface energy across the liquid-solid interface.

**Table 10**: Surface tension parameters for SS316L, Ti–6Al–4V, and Inconel 718 recommended for practical numerical calculations.

| **Parameter name** | **Symbol** | **SS316L** | **Ti–6Al–4V** | **Inconel 718** | **SI unit** |
|---|---|---|---|---|---|
| Surface tension at the liquidus point | $\gamma(T_m)$ | 1.67 | 1.461 | 1.882 | N m$^{-1}$ |
| Thermal coefficient of surface tension | $d\gamma/dT$ | $4.0 \times 10^{-4}$ | $-4.0 \times 10^{-4}$ | $-3.7 \times 10^{-4}$ | N m$^{-1}$ K$^{-1}$ |
| Melting temperature (liquidus) | $T_m$ | 1713 | 1921 | 1609 | K |

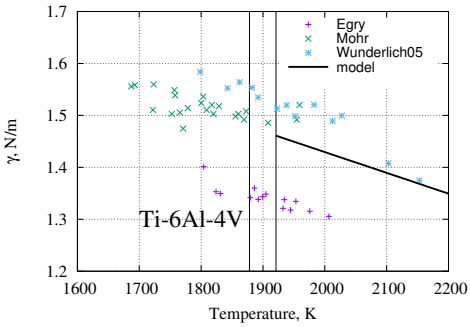
### 3.7.1 Discussion on SS316L

In commercial metal production, the SS316L stainless steel matrix is most frequently contaminated with trace concentrations of sulfur or interstitial oxides [137, 146, 147]. In foundational studies rooted in metallurgical thermodynamics [148], a specialized nonlinear expression has been proposed to describe the functional dependence of surface tension on temperature alongside sulfur and oxygen mass fractions [137, 147]. This comprehensive approach integrates a regular correction to the interfacial energy that



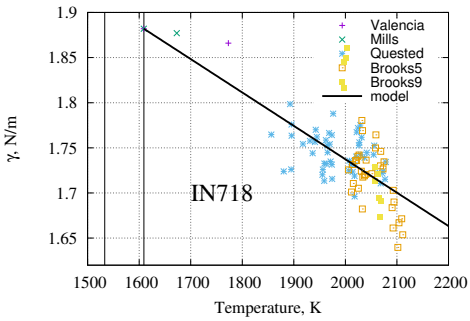

(a) SS316L

**References**
Fukuyama (DSC, electromagnetic levitation, and oscillating drop method) [65], Grant (levitated drop method) [129], Mills (levitated drop method) [5], and Keene (levitated drop method) [66].




(b) Ti–6Al–4V

**References**
Egry (electromagnetic levitation) [143], Mohr (containerless electromagnetic levitation on board the International Space Station) [42], Wunderlich (oscillating drop technique under reduced gravity conditions) [39], and Wunderlich (oscillating drop method on board parabolic flights) [40].




(c) Inconel 718

**References**
Mills (data compilation review) [58], Quested (levitated drop method) [38], Brooks (levitated drop method) [37], and Overfelt (oscillating vessel technique) [36].

**Figure 8**: Calculated regression lines and compiled literature data on the liquid-gas surface tension. The solidus $T_{\mathrm{sol}}$ and liquidus $T_m$ temperatures are designated by vertical lines.

directly correlates with the chemical activity of dissolved oxygen and sulfur impurities according to:

$$\textbf{SS316L}: \gamma(T) = \gamma(T_m) + A(T - T_m) - RT\left[\Gamma_s \ln(1 + K_s a_s) + \Gamma_o \ln(1 + K_o a_o)\right], \quad (27)$$

where $R$ is the universal gas constant, $\gamma(T_m) = 1.77$ N m$^{-1}$ represents the reference surface tension at the melting point, $A = -4.3 \times 10^{-4}$ N m$^{-1}$ K$^{-1}$ is the baseline temperature coefficient evaluated for high-purity (desulfurized) SS316L, while $a_s$ and $a_o$ denote the thermodynamic activities (or concentrations in wt.%) of the dissolved sulfur and oxygen elements, respectively.

The equilibrium constants of impurity segregation are further defined by

$$K_s = k_{1,s} \exp\left(-\frac{\Delta H_s}{RT}\right), \qquad K_o = k_{1,o} \exp\left(-\frac{\Delta H_o}{RT}\right). \quad (28)$$

Here $k_{1,s} = 0.00318$ and $k_{1,o} = 0.0138$ are the entropic factors, $\Delta H_s = -1.66 \times 10^5$ J mol$^{-1}$ and $\Delta H_o = -1.463 \times 10^5$ J mol$^{-1}$ are the standard adsorption heats of sulfur and oxygen, $\Gamma_s = 1.3 \times 10^{-5}$ mol m$^{-2}$ and $\Gamma_o = 2.03 \times 10^{-5}$ mol m$^{-2}$ represent the surface excess amount of both additions.

The calculated values of $\gamma$ and $d\gamma/dT$ for SS316L are obtained at sulfur and oxygen concentrations of 0.03 wt.% (300 ppm) and 0.01 wt.% (100 ppm), respectively, as illustrated in Fig. 9. If the temperature elevates from 1800 K to 2400 K, the effective $\gamma$ value increases from 0.75 to 1.33 N m$^{-1}$, yielding $d\gamma/dT > 0$ at the specified chemical composition. This anomalous behavior is fundamentally explained by the temperature-driven desorption of surface-active constituents. Under intensive heating, the adsorbed sulfur and oxygen atoms evaporate completely from the melt interface. Consequently, the surface tension switches back to the regular baseline behavior typical for an impurity-free refined melt.

Then, above 2400 K and up to 2900 K, $\gamma$ decreases from 1.33 to 1.20 N m$^{-1}$. This downward trend perfectly corresponds to the negative $d\gamma/dT$ behavior expected for desulfurized matrices. Thus, the comprehensive $\gamma(T)$ approximation framework for commercial SS316L reveals a distinct non-monotonic dependence on temperature, where the local maximum of $\gamma(T)$ is reached at $T \approx 2400$ K [149].

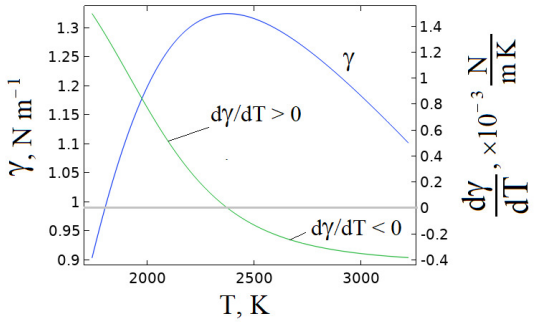



**Figure 9**: Non-monotonic temperature dependence of the effective surface tension $\gamma$ for the SS316L alloy at high sulfur (0.03 wt.%, 300 ppm) and oxygen (0.01 wt.%, 100 ppm) concentrations, as originally revealed in [147] and discussed in [149].

### 3.7.2 Discussion on Ti–6Al–4V

The highly reactive nature of the Ti–6Al–4V melt introduces severe methodological challenges. Therefore, high-precision measurements of its surface tension are typically performed utilizing containerless processing methods, such as electromagnetic levitation. A recent microgravity study conducted onboard the International Space Station (ISS) [42] provides exceptionally accurate data on $\gamma(T)$ within the temperature window between 1700 K and 1950 K, which is well fitted by the linear function:

$$\textbf{Ti–6Al–4V}: \gamma(T) = (1.493 \pm 0.008) - (1.9 \pm 0.5) \times 10^{-4} \cdot (T - 1933) \quad (\text{N m}^{-1}). \quad (29)$$

The registered stable linearity in $\gamma(T)$ is attributed to a low initial oxygen level and the decay of competing adsorption processes. The performed mathematical extension of Eq. (29) to higher-order polynomials has retained the same statistical accuracy of approximation. In sharp contrast to the contaminated SS316L system, this ternary alloy does not demonstrate a sign change of $d\gamma/dT$ within the measured temperature range.

However, the obtained onboard ISS value of $d\gamma/dT = -1.9 \times 10^{-4}$ N m$^{-1}$ K$^{-1}$ [42] differs by a factor of two from the baseline value compiled in Table 10. Diverse literature data (see [150] and references therein) confirm that the track hydrodynamics during the additive manufacturing of Ti–6Al–4V are strongly affected by the partial oxygen pressure inside the processing chamber. This chemical sensitivity explains the notable discrepancy from previous ground-based tests [39, 40] performed via the oscillating drop method onboard parabolic flights. Hence, the ambient $O_2$ level must be thoroughly examined and tracked in both $\gamma$ and $d\gamma/dT$ input functions for numerical multiphysics simulations.

### 3.7.3 Discussion on Inconel 718

The nickel-based superalloy Inconel 718 represents a complex multi-component system, making the experimental evaluation of its surface tension exceptionally difficult. As demonstrated in foundational metallurgical works [37, 43], the melt surface of Inconel 718 is highly prone to the rapid formation of $Cr_2O_3$ and NiO oxide surface films characterized by high mechanical strength. These surface oxide films retain their structural rupture strength up to extreme temperatures of $T \approx 1750°$C. The recommended regular approximation [37] for an Inconel 718 melt containing approximately 10 ppm of trace sulfur is expressed as:

$$\textbf{Inconel 718}\text{: } \gamma(T) = 1.842 - 1.1 \times 10^{-4} \cdot (T - 1998) \quad (\text{N m}^{-1}). \tag{30}$$

The linear regression model expressed in Eq. (30) remains strictly valid only for highly overheated melts where $T > 1725°\mathrm{C}$. Its direct extrapolation to lower temperature boundary fields common to track boundaries in metal AM must carefully incorporate the purity conditions of the protective shielding atmosphere. The resulting thermal coefficient of Inconel 718 ($d\gamma/dT = -0.11 \times 10^{-3}$ N m$^{-1}$ K$^{-1}$) is substantially smaller compared to pure liquid nickel matrices. This stabilizing transport feature is directly attributed to complex alloying by refractory elements, which actively behave as surface-stabilizing active impurities.

## 3.8 Viscosity $\mu$

The viscosity of metallic melts is typically monotonically dependent on temperature. This behavior follows from the fact that viscosity can be fundamentally considered as a generalized transport characteristic related to momentum transfer at the molecular level. On the other hand, the momentum flux in viscous media depends on the frequency of molecular jumps, which is a direct function of temperature. Therefore, metallic melts that do not undergo any anomalous structural transformations in their localized short-range order comply with one of the following functional relationships:

1. the Arrhenius equation [151] for single-phase liquid melts, valid if the temperature exceeds the liquidus point $T_m$ or if the melt is undercooled below $T_m$,
2. the Hirai regression model [152], implemented in scenarios where the melt undergoes active solidification and behaves as a semi-solid slurry.

Under thermal boundary conditions common to industrial casting, the undercooling level rarely exceeds a few Kelvins. Greater undercoolings approaching several hundred Kelvins can be achieved during containerless solidification processing [153]. However, the viscosity of undercooled melts strictly complies with the Arrhenius relation even in deeply undercooled states, as confirmed by robust electromagnetic levitation and free-drop experiments onboard parabolic flights [41].

The viscosity of light liquid metals typically varies within the range of 1–3 mPa·s, whereas iron-based melts yield a baseline viscosity between 5 and 15 mPa·s when evaluated near the liquidus point. As the melt temperature elevates, its effective viscosity drops according to the Arrhenius relation. This framework incorporates a joint functional dependence on both chemical composition and temperature through the expression:

$$\frac{\mu(T)}{\rho(T)} = A \exp\left(\frac{E_\mathrm{a}}{RT}\right), \tag{31}$$

where $\mu$ represents the dynamic viscosity, $A$ is the pre-exponential kinetic factor, $E_{\mathrm{a}}$ is the activation energy specific to the alloy configuration, $R$ is the universal gas constant, $T$ is the absolute temperature, and $\rho(T)$ is the temperature-dependent density. Generally, the transport parameters $A$ and $E_{\mathrm{a}}$ are extrapolated from empirical kinematic viscosity curves ($\mu/\rho = f(T)$) obtained via high-temperature oscillating viscosimetry [154, 155].

Once the melt undergoes solidification, it must be mathematically treated as a two-phase mushy mixture [156]. Owing to solute redistribution ahead of the moving solidification front, the local viscosity of the remaining liquid phase varies slightly; however, this chemical variation rarely exceeds 5–10%. Thus, temperature and solid fraction exert a far more dominant impact on the effective viscosity than local solute segregation.

The apparent viscosity of a semi-solid metal slurry demonstrates a pronounced correlation with the fluid shear rate, exhibiting a sharp decline as the shear rate escalates. Furthermore, it is heavily influenced by the local cooling rate [156]. For practical numerical calculations, the Hirai formulation is highly recommended [152]:

$$\mu_{\text{semi-solid}}(f_S) = \mu_L \left[ 1 + \frac{a}{2\left(\dfrac{1}{f_S} - \dfrac{1}{f_S^{\text{crit}}}\right)} \right], \tag{32}$$

where $\mu_{\text{semi-solid}}$ represents the apparent effective viscosity of the slurry, $\mu_L$ is the dynamic viscosity of the pure liquid phase at the liquidus line, $f_S$ is the local solid fraction varying within the range of $0 \leq f_S \leq 1$, $a$ is a parameter dependent on the fluid shear rate, and $f_S^{\text{crit}}$ is the critical solid fraction at which the semi-solid medium transitions into a super-viscous state. For various industrial alloys, the critical fraction $f_S^{\text{crit}}$ varies between 0.3 and 0.6. Consequently, two distinct transport subintervals of $f_S$ can be emphasized: (1) a solid fraction range of $0 \leq f_S \leq 0.3$ yields a weak,

weakly non-linear rise in viscosity; (2) when $f_S$ exceeds 0.3, the function $\mu(T)$ becomes strongly non-linear as the internal dendritic network begins to impinge.

The parameter $a$ and the critical fraction are directly defined utilizing experimental data on the shear flow of solidifying slurries as follows [152]:

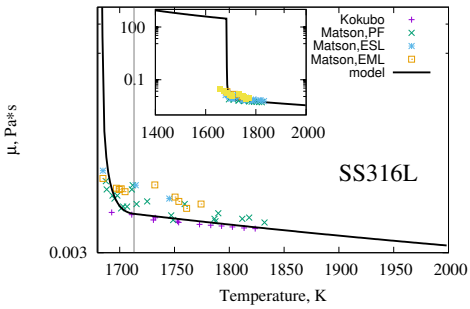
$$\begin{aligned} a &= \alpha \rho_m C^{1/3} \dot{\gamma}_{\mathrm{sh}}^{-4/3}, \quad f_S^{\mathrm{crit}} = 0.72 - \beta C^{-1/3}, \\ \alpha &= 2.03 \times 10^2 \left(\frac{X}{100}\right)^{1/3}, \quad \beta = 19.0 \left(\frac{X}{100}\right)^{1/3}, \end{aligned} \tag{33}$$

where $\rho_m$ represents the density evaluated at the melting point, $C = df_S/dt$ is the solidification rate evaluated within the initial window ($0 \leq f_S \leq 0.4$), $\dot{\gamma}_{\mathrm{sh}}$ is the fluid shear rate, and $X$ denotes the mass percentage of the primary matrix component. The Hirai framework is highly effective for evaluating the rheology of solidifying track regions in metal AM before a fully rigid, interconnected crystalline network is established.

All optimized constants recommended for the Arrhenius (Eq. (31)) and Hirai (Eqs. (32) and (33)) models are compiled in Table 11. The resulting effective viscosity curves evaluated as functions of temperature for the selected alloys are illustrated in Fig. 10.

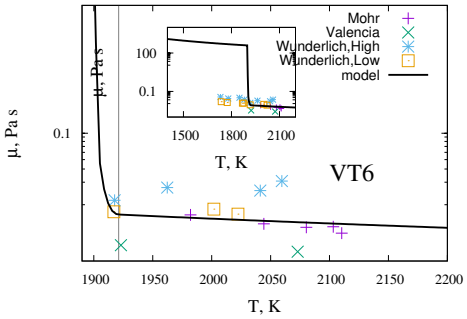
**Table 11**: Viscosity-related validation parameters for the Arrhenius (Eq. (31)) and Hirai (Eqs. (32) and (33)) models recommended for numerical AM simulations.

| **Parameter name** | **Symbol** | **SS316L** | **Ti–6Al–4V** | **Inconel 718** | **SI unit** |
|---|---|---|---|---|---|
| Activation energy (Arrhenius) | $E_{\mathrm{a}}$ | $1.78 \times 10^5$ | $5.10 \times 10^4$ | $5.02 \times 10^4$ | J mol$^{-1}$ |
| Pre-exponential factor (Arrhenius) | $A$ | $6.00 \times 10^{12}$ | $7.68 \times 10^8$ | $2.19 \times 10^8$ | m$^2$ s$^{-1}$ |
| Slurry parameter (Hirai) | $a$ | 1 | 4.5 | 8.76 | – |
| Critical solid fraction (Hirai) | $f_S^{\mathrm{crit}}$ | 0.85 | 0.45 | 0.33 | – |



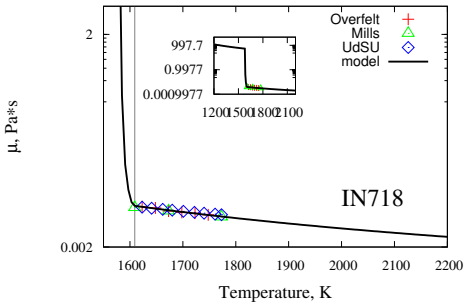

(a) SS316L

**References**
Kokubo (oscillating crucible method) [157], and Matson (parabolic flights, electrostatic levitation, and electromagnetic levitation frameworks) [41].




(b) Ti–6Al–4V

**References**
Mohr (containerless electromagnetic levitation onboard the International Space Station) [42], Valencia (comprehensive review) [72], and Wunderlich (oscillating drop method onboard parabolic flights) [40].




(c) Inconel 718

**References**
Overfelt (oscillating vessel technique) [36], and Mills (recommended thermophysical dataset compilation) [43].

**Figure 10**: Calculated effective dynamic viscosities of (a) SS316L steel, (b) Ti–6Al–4V alloy, and (c) Inconel 718 as functions of temperature $T$. The vertical lines indicate the respective liquidus points.

## 3.9 Young's modulus $E$

The linear relationship between normal stresses and relative linear strains in the initial loading regime of elastic deformation is described by Hooke's law:

$$\begin{aligned} \sigma &= E \cdot \varepsilon, \\ E &= \frac{\sigma}{\varepsilon} = \tan \alpha, \end{aligned} \tag{34}$$

where $E$ represents the proportionality coefficient (Young's modulus), $\sigma$ is the normal stress (Pa), $\varepsilon$ is the relative strain, and $\alpha$ is the slope angle of the linear elastic region on the stress-strain curve.

Young's modulus, or the longitudinal elastic modulus $E$ (Pa), is a mechanical quantity characterizing the capacity of a material to resist uniaxial tension and compression under elastic loading conditions. It is generally formulated as:

$$E = \frac{F \cdot l_0}{A_{\text{cs}} \cdot \Delta l}, \tag{35}$$

where $F$ is the normal component of the applied load, $l_0$ is the initial length of the specimen, $A_{\text{cs}}$ represents the cross-sectional area over which the force is distributed, and $\Delta l$ is the absolute change in length resulting from elastic deformation. The ratio $P = F/A_{\text{cs}}$ characterizes the magnitude of internal normal stresses developing within the deformed material, while $\Delta l/l_0$ represents the engineering strain or specific elongation.

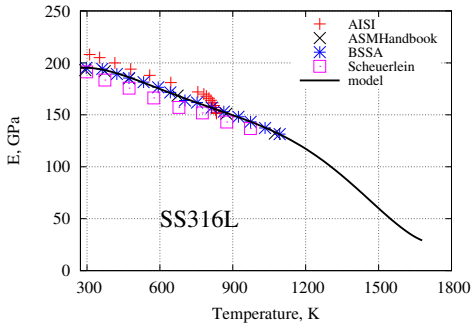
The Wachtman model is an empirical formulation that describes the continuous temperature dependence of Young's modulus $E$ for crystalline and ceramic structures. This framework is widely utilized to capture the non-linear degradation of elastic properties in metallic superalloys at elevated temperatures. Based on experimental trends, the model was originally proposed by Wachtman and subsequently developed

in Refs. [158–160] to evaluate the effective Young's modulus $E(T)$ according to:

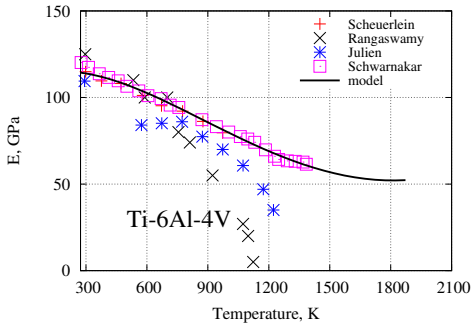
$$E(T) = E_0 - b \cdot T \cdot \exp\left(-\frac{T_0}{T}\right), \tag{36}$$

where $E_0$ represents the theoretical Young's modulus at absolute zero ($T = 0$ K), $b$ is an empirical material parameter, and $T_0$ is a characteristic temperature parameter related to the Debye temperature of the crystalline lattice.

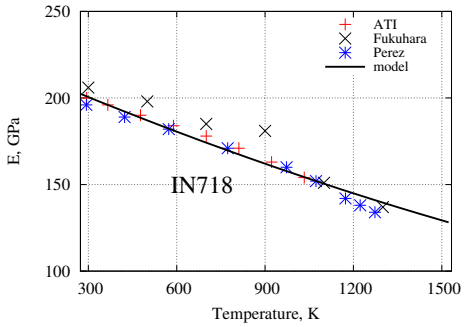
The recommended polynomial models for calculating the temperature-dependent Young's modulus are presented in Fig. 11.




(a) SS316L




(b) Ti–6Al–4V




(c) Inconel 718

**References**

ASM Handbook [161], BSSA [162] (online datasheet), Scheuerlein [163] (in situ heat cycles, dynamic resonance method, push-rod dilatometer), Rangaswamy [164] (neutron diffraction, FE modeling), Julien [165] (mechanical tests with prior in-situ heat treatment), Swarnakar [53] (impulse excitation technique), ATI [166] (datasheet), Fukuhara [64] (ultrasonic pulse sing-around method), and Perez [47] (uniaxial tensile tests, digital image correlation).

**Figure 11**: Young's modulus calculated using the recommended regression model and validation data for (a) SS316L, (b) Ti–6Al–4V, and (c) Inconel 718.

## 3.10 Shear modulus $G$

The shear modulus $G$ (Pa) is a fundamental mechanical property characterizing the capacity of a material to resist shear deformation, and it represents the second Lamé parameter. The shear modulus is defined by the following expression:

$$G = \frac{\tau}{\tan\theta} = \frac{F/A_{\mathrm{cs}}}{\Delta x/l} = \frac{Fl}{A_{\mathrm{cs}}\Delta x}, \tag{37}$$

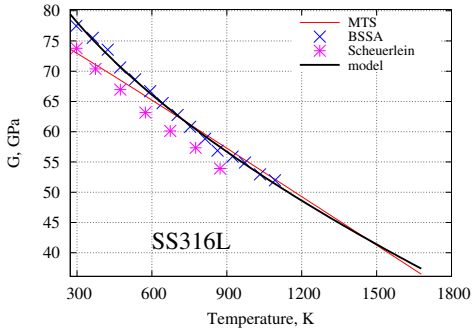
where $\tau = F/A_{\mathrm{cs}}$ is the shear stress, $F$ is the applied force, $A_{\mathrm{cs}}$ is the cross-sectional area over which the force acts, and $\theta$ is the shear strain angle, with $\Delta x/l = \tan\theta$ representing the shear strain where $\Delta x$ is the lateral displacement and $l$ is the initial object length.

The Mechanical Threshold Stress (MTS) model is a well-established theoretical framework describing the dependence of the mechanical properties of materials, including the shear modulus $G$, on temperature, strain rate, and microstructure. The MTS model [167, 168] is widely implemented to analyze the plastic deformation of metals and alloys under high-temperature and dynamic loading conditions. Originally developed within the framework of the MTS plasticity model, it is commonly referred to as the MTS shear modulus model. According to this formulation, the temperature dependence of the shear modulus is defined as:

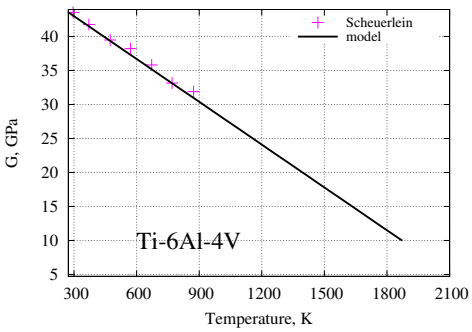
$$G = G_0 - \frac{D}{\exp\left(\dfrac{T_0}{T}\right) - 1}, \tag{38}$$

where $G_0$ represents the reference shear modulus at the baseline temperature, $T_0 = 273$ K, and $D$ is a material-specific empirical constant.

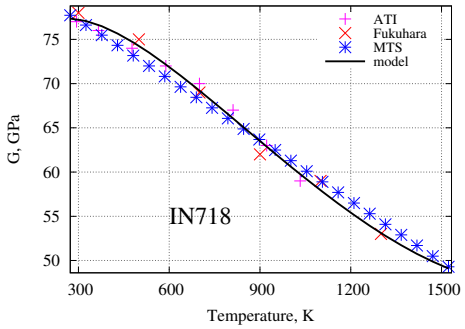
The recommended polynomial models for calculating the temperature-dependent shear modulus are presented in Fig. 12.




(a) SS316L




(b) Ti–6Al–4V




(c) Inconel 718

**References**
BSSA [162] (online datasheet), Scheuerlein [163] (in situ heat cycles, dynamic resonance method, push-rod dilatometer), ATI [166] (datasheet), and Fukuhara [64] (ultrasonic pulse sing-around method).

**Figure 12**: Shear modulus calculated using the recommended regression model and validation data for (a) SS316L, (b) Ti–6Al–4V, and (c) Inconel 718.

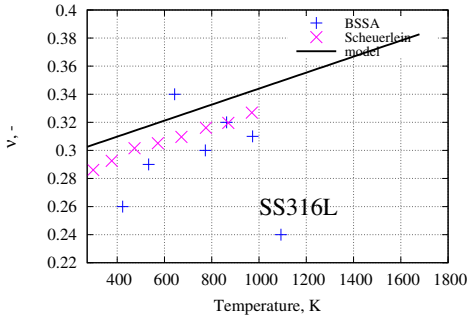
## 3.11 Poisson's ratio $\nu$

Poisson's ratio $\nu$ is a dimensionless mechanical characteristic of a material that defines the ratio of relative transverse compression to relative longitudinal extension under elastic deformation:

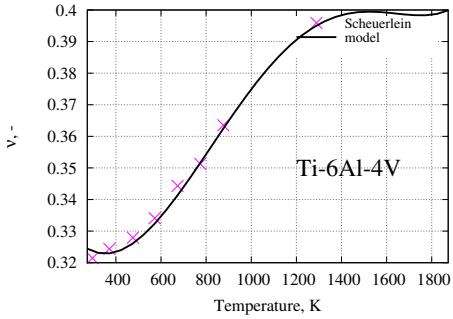
$$\nu = -\frac{\varepsilon'}{\varepsilon} = -\frac{\Delta d/d_0}{\Delta l/l_0}, \tag{39}$$

where $\varepsilon' = \Delta d/d_0$ is the relative transverse strain (change relative to the initial diameter or width), and $\varepsilon = \Delta l/l_0$ is the relative longitudinal strain (change in length relative to the initial length). The minus sign is introduced because during tensile deformation ($\varepsilon > 0$), the transverse dimensions decrease ($\varepsilon' < 0$), ensuring that the

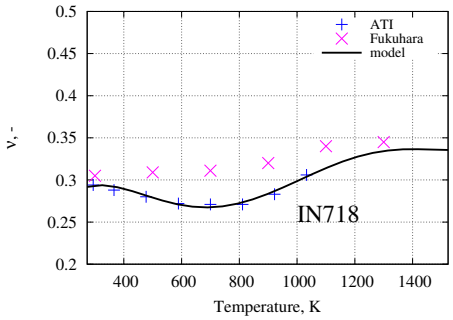
ratio remains positive for most engineering materials. The recommended polynomial models for calculating Poisson's ratio are presented in Fig. 13.




(a) SS316L




(b) Ti–6Al–4V




(c) Inconel 718

**References**
BSSA [162] (online datasheet), Scheuerlein [163] (in situ heat cycles, dynamic resonance method, push-rod dilatometer), ATI [166] (datasheet), and Fukuhara [64] (ultrasonic pulse sing-around method).

**Figure 13**: Poisson's ratio calculated using the recommended regression model and validation data for (a) SS316L, (b) Ti–6Al–4V, and (c) Inconel 718.

## 3.12 Yield strength $\sigma_{0.2}$

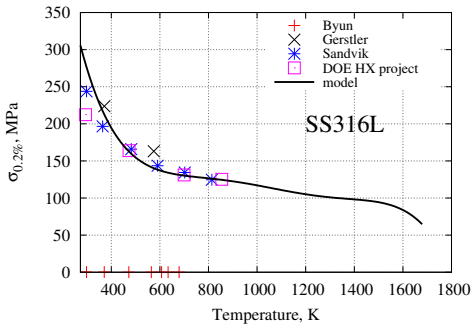
The 0.2% yield strength ($\sigma_{0.2}$) is the stress at which a material begins to plastically deform, reaching 0.2% of its original length. This parameter is typically used for the evaluation of strength and deformability of materials that do not have a clear yield

point. The 0.2% yield strength can be determined using the following formula:

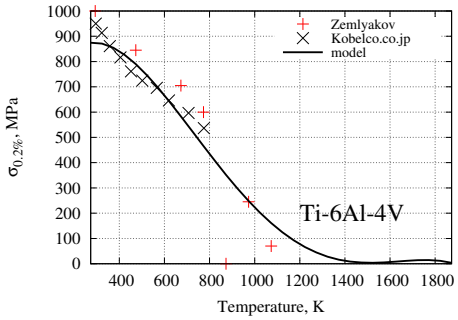
$$\sigma_{0.2} = \frac{F}{A_0}, \tag{40}$$

where $\sigma_{0.2}$ is the 0.2% yield strength (Pa), $F$ is the force applied to the specimen (N), and $A_0$ is the initial cross-sectional area of the specimen ($m^2$).

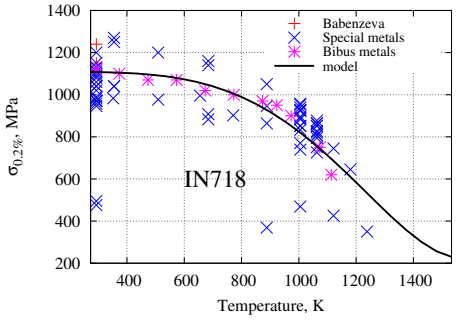
The 0.2% offset yield strength on a stress-strain curve is typically identified by the point aligning with 0.2% permanent strain on the horizontal axis. The recommended polynomial models for calculating the 0.2% yield strength are presented in Fig. 14.




(a) SS316L




(b) Ti–6Al–4V




(c) Inconel 718

**References**

Byun [169] (tensile and Charpy impact testing), Gerstler [170] (tensile tests), Sandvik [171] (materials datasheet), Zemlyakov [172] (tensile test at room temperature), Babentsova [173] (low-cycle fatigue tests, high-temperature extensometer), Special Metals [174] (datasheet), Bibus Metals [175] (datasheet), and Kobelco [176] (datasheet).

**Figure 14**: 0.2% yield strength calculated using the recommended regression model and validation data for (a) SS316L, (b) Ti–6Al–4V, and (c) Inconel 718.

The selection of the optimal polynomial degree was conducted using a unified algorithm based on the following information criteria:

1) Akaike information criterion (AIC):

$$AIC = 2k - n \cdot \ln\left(\frac{RSS}{n}\right), \tag{41}$$

$$RSS = \sum_{i=1}^{N}(y_i - \overline{y_i})^2, \tag{42}$$

where $k$ is the number of model parameters, $n$ is the number of points, $RSS$ is the residual sum of squares calculated by Eq. (42), $y_i$ represents the experimental points, $\overline{y_i}$ stands for the values generated by the polynomial model, and $N$ is the total number of data points.

2) Bayesian information criterion (BIC):

$$BIC = \ln n \cdot k - n \cdot \ln\left(\frac{RSS}{n}\right), \tag{43}$$

3) Hannan-Quinn criterion (HQC):

$$HQC = 2\ln(\ln(n)) \cdot k - n \cdot \ln\left(\frac{RSS}{n}\right). \tag{44}$$

For each temperature dependence, polynomial models were sequentially calculated over a degree range from $-5$ to 5 (including both positive and negative powers to analyze inverse dependencies). Subsequently, for each model, the AIC, BIC, and HQC values were determined. The optimal model was selected by minimizing these criteria, balancing fitting accuracy and model complexity. All calculation results are summarized in Table 12.

## Funding

The work was supported by the Ministry of Science and Higher Education of the Russian Federation [the state grant number 124021900019-5]. A part of this study was funded within the projects EOTP-MT-097 and Ph.D. grant SPN.2024.03151.

## Appendix A Tabulated thermophysical and mechanical properties at different temperatures

This section contains the tabular data for all thermophysical and mechanical properties of SS316L, Ti–6Al–4V and Inconel 718 as a function of temperature. The properties are calculated using the recommended piece-wise polynomial models derived in the present paper. The listed below characteristics are split in two tables over different temperature intervals: (1) between the room and solidus temperatures, (2) between the solidus and boiling temperatures.

## References

[1] Shishkovsky, I.V.: Laser Synthesis of Functionally Graded Mesostructures and Three-Dimensional Products. Fizmatlit, Moscow (2009)

[2] Shishkovsky, I.V.: Fundamentals of High-Resolution Additive Technologies. Nauka, Moscow (2016)

[3] Brandt, M. (ed.): Laser Additive Manufacturing. Woodhead Publishing, Cambridge, England (2016)

[4] Gu, D.: Laser Additive Manufacturing of High-performance Materials. Springer, New York, NY (2015)

[5] Mills, K.C., Brooks, R.F.: Measurements of thermophysical properties in high temperature melts. Materials Science and Engineering: A **178**(1-2), 77–81 (1994) https://doi.org/10.1016/0921-5093(94)90522-3

[6] Li, Z., Mukai, K., Zeze, M., Mills, K.C.: Determination of the surface tension of liquid stainless steel. Journal of Materials Science **40**(9-10), 2191–2195 (2005) https://doi.org/10.1007/s10853-005-1931-x

[7] Boivineau, M., Cagran, C., Doytier, D., Eyraud, V., Nadal, M.-H., Wilthan, B., Pottlacher, G.: Thermophysical Properties of Solid and Liquid Ti-6Al-4V (TA6V) Alloy. International Journal of Thermophysics **27**(2), 507–529 (2006) https://doi.org/10.1007/PL00021868

[8] Wei, L.C., Ehrlich, L.E., Powell-Palm, M.J., Montgomery, C., Beuth, J., Malen, J.A.: Thermal conductivity of metal powders for powder bed additive manufacturing. Additive Manufacturing **21**, 201–208 (2018) https://doi.org/10.1016/j.addma.2018.02.002

[9] Widenfeld, G., Weiss, Y., Kalman, H.: The effect of compression and preconsolidation on the effective thermal conductivity of particulate beds. Powder Technology **133**(1-3), 15–22 (2003) https://doi.org/10.1016/S0032-5910(03)00096-0

[10] Rombouts, M., Froyen, L., Gusarov, A.V., Bentefour, E.H., Glorieux, C.: Photopyroelectric measurement of thermal conductivity of metallic powders. Journal of Applied Physics **97**(2), 024905 (2005) https://doi.org/10.1063/1.1832741

[11] Lima, W.M., Biondo, V., Weinand, W., Nogueira, E., Medina, A., Baesso, M., Bento, A.: The effect of porosity on thermal properties: Towards a threshold of particle contact in sintered stainless steel. Journal of Physics: Condensed Matter

**17**, 1239 (2005) https://doi.org/10.1088/0953-8984/17/7/016

[12] Williams, J.D., Deckard, C.R.: Advances in modeling the effects of selected parameters on the SLS process. Rapid Prototyping Journal **4**, 90–100 (1998) https://doi.org/10.1108/13552549810210257

[13] Gibson, I., Rosen, D., Stucker, B., Khorasani, M.: Additive Manufacturing Technologies. Springer, ??? (2021). https://doi.org/10.1007/978-3-030-56127-7

[14] Meier, C., Penny, R.W., Zou, Y., Gibbs, J.S., Hart, A.J.: Thermophysical Phenomena in Metal Additive Manufacturing By Selective Laser Melting: Fundamentals, Modeling, Simulation, and Experimentation. Annual Review of Heat Transfer **20**, 241–316 (2017) https://doi.org/10.1615/AnnualRevHeatTransfer.2018019042

[15] Khairallah, S.A., Martin, A.A., Lee, J.R.I., Guss, G., Calta, N.P., Hammons, J.A., Nielsen, M.H., Chaput, K., Schwalbach, E., Shah, M.N., Chapman, M.G., Willey, T.M., Rubenchik, A.M., Anderson, A.T., Wang, Y.M., Matthews, M.J., King, W.E.: Controlling interdependent meso-nanosecond dynamics and defect generation in metal 3D printing. Science **368**, 660–665 (2020) https://doi.org/10.1126/science.aay7830

[16] King, W.E., Anderson, A.T., Ferencz, R.M., Hodge, N.E., Kamath, C., Khairallah, S.A., Rubenchik, A.M.: Laser powder bed fusion additive manufacturing of metals; physics, computational, and materials challenges. Applied Physics Reviews **2**, 041304 (2015) https://doi.org/10.1063/1.4937809

[17] Liu, L., Huang, M., Ma, Y.H., Qin, M.L., Liu, T.T.: Simulation of Powder Packing and Thermo-Fluid Dynamic of 316L Stainless Steel by Selective Laser Melting. Journal of Materials Engineering and Performance **29**, 7369–7381

(2020) https://doi.org/10.1007/s11665-020-05230-w

[18] Li, E., Zhou, Z., Wang, L., Zou, R., Yu, A.: Particle scale modelling of powder recoating and melt pool dynamics in laser powder bed fusion additive manufacturing: A review. Powder Technology **409**, 117789 (2022) https://doi.org/10.1016/j.powtec.2022.117789

[19] Tang, D., Hu, Y., Yang, L., Yan, C., Shi, Y.: Melt Pool Simulation Technology of Laser Powder Bed Fusion: A Review. Jom **76**, 4663–4682 (2024) https://doi.org/10.1007/s11837-024-06699-9

[20] Ankudinov, V., Gordeev, G.A.A., Krivilyov, M.D.D.: Numerical simulation of heat transfer and melting of Fe-based powders in SLM processing. IOP Conference Series: Materials Science and Engineering **192**, 12026 (2017) https://doi.org/10.1088/1757-899X/192/1/012026

[21] Gordeev, G.A., Ankudinov, V., Kharanzhevskiy, E.V., Krivilyov, M.D.: Numerical simulation of selective laser melting with local powder shrinkage using FEM with the refined mesh. The European Physical Journal Special Topics **229**, 205–216 (2020) https://doi.org/10.1140/epjst/e2019-900100-6

[22] Ankudinov, V., Gordeev, G., Kharanzhevskiy, E.V., Galenko, P.K.: Formation of temperature-induced defects in the multiscale model of ceramic glazes sintering. Journal of Physics: Condensed Matter **37**, 485402 (2025) https://doi.org/10.1088/1361-648X/ae217c

[23] Hsu, C.-T., Cheng, P., Wong, K.W.: Modified Zehner-Schlünder models for stagnant thermal conductivity of porous media. Journal of Porous Media **37**(1), 19–38 (1994)

[24] Kaviany, M.: Principles of Heat Transfer in Porous Media. Springer, ??? (1995)

[25] Lykov, A.V.: Theory of Thermal Conductivity (1967)

[26] Zehnder, P., Schlünder, E.U.: Wärmeleitfähigkeit von Schüttungen bei mäßigen Temperaturen. Chemie Ingenieur Technik **42**, 933–941 (1970) https://doi.org/10.1002/cite.330421408

[27] Ankudinov, V., Gordeev, G.A., Kharanzhevskiy, E.V., Krivilyov, M.D.: Numerical Simulation of Thermal Conductivity of Stainless Steel and Al-12Si Powders for Additive Manufacturing. Journal of Heat Transfer **144**(5), 1–31 (2022) https://doi.org/10.1115/1.4053853

[28] Kunii, D., Smith, J.M.: Heat transfer characteristics of porous rocks. AIChE Journal **6**(1), 71–78 (1960) https://doi.org/10.1002/aic.690060115

[29] Agazhanov, A.S., Samoshkin, D.A., Kozlovskii, Y.M.: Thermophysical properties of Inconel 718 alloy. Journal of Physics: Conference Series **1382**(1), 012175 (2019) https://doi.org/10.1088/1742-6596/1382/1/012175

[30] Lee, S.H., Kim, S.W., Kang, K.H.: Effect of Heat Treatment on the Specific Heat Capacity of Nickel-Based Alloys. International Journal of Thermophysics **27**(1), 282–292 (2006) https://doi.org/10.1007/s10765-006-0029-2

[31] Hosaeus, H., Seifter, A., Kaschnitz, E., Pottlacher, G.: Thermophysical properties of solid and liquid Inconel 718 alloy. High Temperatures - High Pressures **33**(4), 405–410 (2001)

[32] Wilthan, B., Reschab, H., Tanzer, R., Schützenhöfer, W., Pottlacher, G.: Thermophysical Properties of a Chromium-Nickel-Molybdenum Steel in the Solid and Liquid Phases. International Journal of Thermophysics **29**(1), 434–444 (2008) https://doi.org/10.1007/s10765-007-0300-1

[33] Pottlacher, G., Hosaeus, H., Kaschnitz, E., Seifter, A.: Thermophysical properties of solid and liquid Inconel 718 Alloy. Scandinavian Journal of Metallurgy **31**(3), 161–168 (2002) https://doi.org/10.1034/j.1600-0692.2002.310301.x

[34] Basak, D., Overfelt, R.A., Wang, D.: Measurement of Specific Heat Capacity and Electrical Resistivity of Industrial Alloys Using Pulse Heating Techniques. International Journal of Thermophysics **24**(6), 1721–1733 (2003) https://doi.org/10.1023/B:IJOT.0000004101.88449.86

[35] Kaschnitz, E., Reiter, P., McClure, J.L.: Thermophysical Properties of Solid and Liquid 90Ti-6Al-4V. International Journal of Thermophysics **23**(1), 267–275 (2002) https://doi.org/10.1023/A:1013925715428

[36] Overfelt, R.A., Matlock, C.A., Wells, M.E.: Viscosity of superalloy 718 by the oscillating vessel technique. Metallurgical and Materials Transactions B **27**(4), 698–701 (1996) https://doi.org/10.1007/BF02915672

[37] Brooks, R.F., Monaghan, B., Barnicoat, A.J., McCabe, A., Mills, K.C., Quested, P.N.: The physical properties of alloys in the liquid and mushy states. International Journal of Thermophysics **17**(5), 1151–1161 (1996) https://doi.org/10.1007/BF01442002

[38] Quested, P.N., Brooks, R.F., Chapman, L., Morrell, R., Youssef, Y., Mills, K.C.: Measurement and estimation of thermophysical properties of nickel based superalloys. Materials Science and Technology **25**(2), 154–162 (2009) https://doi.org/10.1179/174328408X361454

[39] Aune, R., Battezzati, L., Brooks, R., Egry, I., Fecht, H.-J., Garandet, J.-P., Mills, K., Passerone, A., Quested, P., Ricci, E., Schneider, S., Seetharaman, S., Wunderlich, R., Vinet, B.: Surface Tension and Viscosity of Industrial Alloys

from Parabolic Flight Experiments. Microgravity - Science and Technology **16**, 11–14 (2005) https://doi.org/10.1007/BF02945937

[40] Wunderlich, R.: Surface Tension and Viscosity of Industrial Ti-Alloys Measured by the Oscillating Drop Method on Board Parabolic Flights. High Temperature Materials and Processes **27**(6), 401–412 (2008) https://doi.org/10.1515/HTMP.2008.27.6.401

[41] Matson, D., Xiao, X., Rodriguez, J., Wunderlich, R.: Preliminary experiments using electromagnetic levitation on the international space station. International Journal of Microgravity Science and Application **33**(2), 330206 (2016) https://doi.org/10.15011/jasma.33.330206

[42] Mohr, M., Wunderlich, R., Novakovic, R., Ricci, E., Fecht, H.-J.: Precise measurements of thermophysical properties of liquid Ti-6Al-4V (Ti64) alloy on board the international space station. Advanced Engineering Materials **22**(7), 2000169 (2020) https://doi.org/10.1002/adem.202000169

[43] Mills, K.C.: Recommended Values of Thermophysical Properties for Selected Commercial Alloys. Woodhead Publishing, Cambridge (2002)

[44] Touloukian, Y.S., *et al.*: Thermophysical Properties of Matter, the TPRC Data Series. IFI-Plenum, New York (1970)

[45] IAEA: Thermophysical Properties Database of Materials for Light Water Reactors and Heavy Water Reactors. IAEA TECDOC Series. IAEA, Vienna, Austria (2006)

[46] Weeks, T., Derimow, N., Benzing, J.: Tensile tests at 77 K and 4 K on 316L stainless steel welded plates. Technical report, National Institute of Standards and Technology, Gaithersburg, MD (2022). https://doi.org/10.6028/NIST.IR.

8438

[47] Pérez Caro, L., Odenberger, E.-L., Schill, M., Niklasson, F., Åkerfeldt, P., Oldenburg, M.: Springback prediction and validation in hot forming of a double-curved component in alloy 718. International Journal of Material Forming **14**(6), 1355–1373 (2021) https://doi.org/10.1007/s12289-021-01615-x

[48] Xu, M., Guo, H., Wang, Y., Hou, Y., Dong, Z., Zhang, L.: Mechanical properties and microstructural characteristics of 316L stainless steel fabricated by laser powder bed fusion and binder jetting. Journal of Materials Research and Technology **24**, 4427–4439 (2023) https://doi.org/10.1016/j.jmrt.2023.04.072

[49] Khan, S.Z., Khan, T.M., Joya, Y.F., Khan, M.A., Ahmed, S., Shah, A.: Assessment of material properties of AISI 316L stainless steel using non-destructive testing. Nondestructive Testing and Evaluation **31**(4), 360–370 (2016) https://doi.org/10.1080/10589759.2015.1121266

[50] Kim, C., Yin, H., Shmatok, A., Prorok, B.C., Lou, X., Matlack, K.H.: Ultrasonic nondestructive evaluation of laser powder bed fusion 316L stainless steel. Additive Manufacturing **38**, 101800 (2021) https://doi.org/10.1016/j.addma.2020.101800

[51] Moretti, M.A., Dalai, B., Åkerström, P., Arvieu, C., Jacquin, D., Lacoste, E., Lindgren, L.-E.: High strain rate deformation behavior and recrystallization of alloy 718. Metallurgical and Materials Transactions A **52**(12), 5243–5257 (2021) https://doi.org/10.1007/s11661-021-06467-9

[52] Yusuf, S., Chen, Y., Boardman, R., Yang, S., Gao, N.: Investigation on porosity and microhardness of 316L stainless steel fabricated by selective laser melting. Metals **7**(2), 64 (2017) https://doi.org/10.3390/met7020064

[53] Swarnakar, A.K., Biest, O., Baufeld, B.: Young's modulus and damping in dependence on temperature of Ti-6Al-4V components fabricated by shaped metal deposition. Journal of Materials Science **46**(11), 3802–3811 (2011) https://doi.org/10.1007/s10853-011-5299-9

[54] Iturbe, A., Giraud, E., Hormaetxe, E., Garay, A., Germain, G., Ostolaza, K., Arrazola, P.J.: Mechanical characterization and modelling of Inconel 718 material behavior for machining process assessment. Materials Science and Engineering A **682**, 441–453 (2017) https://doi.org/10.1016/j.msea.2016.11.054

[55] Park, H.-W., Kakiuchi, S., Kim, K., Yanagida, A., Yanagimoto, J.: Constitutive equation for flow stress in superalloy 718 by inverse analysis under hot forming in a region of precipitation. Crystals **11**(7), 811 (2021) https://doi.org/10.3390/cryst11070811

[56] Mills, K.C.: Fe - 316 Stainless Steel. In: Mills, K.C. (ed.) Recommended Values of Thermophysical Properties for Selected Commercial Alloys, pp. 135–142. Woodhead Publishing, ??? (2002). https://doi.org/10.1533/9781845690144.135

[57] Mills, K.C.: Ti-6Al-4V. In: Mills, K.C. (ed.) Recommended Values of Thermophysical Properties for Selected Commercial Alloys, pp. 54–57. Woodhead Publishing, ??? (2002). https://doi.org/10.1533/9781845690144.54

[58] Mills, K.C.: Ni - IN 718, pp. 181–190. Woodhead Publishing, ??? (2002). https://doi.org/10.1533/9781845690144.181

[59] Bogaard, R.H., Desai, P.D., Li, H.H., Ho, C.Y.: Thermophysical properties of stainless steels. Thermochimica Acta **218**, 373–393 (1993) https://doi.org/10.1016/0040-6031(93)80437-F

[60] Brooks, R.F., Day, A.P., Mills, K.C., Quested, P.N.: Physical property measurements for the mathematical modeling of fluid flow in solidification processes. International Journal of Thermophysics **18**(2), 471–480 (1997) https://doi.org/10.1007/BF02575176

[61] Brooks, R., Day, A., Andon, R., Chapman, L., Mills, K., Quested, P.: Measurement of viscosities of metals and alloys with an oscillating viscometer. High Temperatures-High Pressures **33**(1), 73–82 (2001) https://doi.org/10.1068/htwu139

[62] Brooks, R., Robinson, J., Chapman, L., Richardson, M.: The enthalpy of a solid and liquid titanium-aluminium-vanadium alloy. High Temperatures-High Pressures **35/36**(2), 193–198 (2003) https://doi.org/10.1068/htjr059

[63] Egry, I., Holland-Moritz, D., Novakovic, R., Ricci, E., Wunderlich, R., Sobczak, N.: Thermophysical Properties of Liquid AlTi-Based Alloys. International Journal of Thermophysics **31**, 949–965 (2010) https://doi.org/10.1007/s10765-010-0704-1

[64] Fukuhara, M., Sanpei, A.: Elastic moduli and internal frictions of Inconel 718 and Ti-6Al-4V as a function of temperature. Journal of Materials Science Letters **12**(14), 1122–1124 (1993) https://doi.org/10.1007/BF00420541

[65] Fukuyama, H., Higashi, H., Yamano, H.: Thermophysical Properties of Molten Stainless Steel Containing 5 mass% B4C. Nuclear Technology **205**, 1154–1165 (2019) https://doi.org/10.1080/00295450.2019.1578572

[66] Keene, B.J., Mills, K.C., Kasama, A., McLean, A., Miller, W.A.: Comparison of surface tension measurements using the levitated droplet method. Metallurgical Transactions B **17**(1), 159–162 (1986) https://doi.org/10.1007/BF02670828

[67] Pehlke, R., Jeyarajan, A., Wada, H.: Summary of Thermal Properties for Casting Alloys and Mold Materials. NASA STI/Recon Technical Report N **83**, 36293 (1982)

[68] Pichler, P., Simonds, B.J., Sowards, J.W., Pottlacher, G.: Measurements of thermophysical properties of solid and liquid NIST SRM 316L stainless steel. Journal of Materials Science **55**(9), 4081–4093 (2020) https://doi.org/10.1007/s10853-019-04261-6

[69] Pichler, P., Leitner, T., Kaschnitz, E., Rattenberger, J., Pottlacher, G.: Surface tension and thermal conductivity of NIST SRM 1155a (AISI 316L stainless steel). International Journal of Thermophysics **43**(5) (2022) https://doi.org/10.1007/s10765-022-03002-x

[70] Pottlacher, G.: Beiträge zur experimentellen Untersuchung thermophysikalischer Daten flüssiger Metalle und Legierungen. PhD thesis, Technische Universität Graz (1998)

[71] Quested, P.N., Mills, K.C., Brooks, R.F., Monaghan, B.J., Dinsdale, A.T., Day, A.R., Richardson, M.J., Andon, R.J.L., Taylor, R., Szelagowski, H.: Physical property measurements for the mathematical modelling of heat and fluid flow in solidification processes. International Journal of Thermophysics **18**, 471–480 (1998) https://doi.org/10.1007/BF02575176

[72] Valencia, J.J., Quested, P.N.: Thermophysical Properties. In: Metals Process Simulation. ASM International, ??? (2010). https://doi.org/10.31399/asm.hb.v22b.a0005523

[73] Hadley, G.R.: Thermal conductivity of packed metal powders. International Journal of Heat and Mass Transfer **29**(6), 909–920 (1986) https://doi.org/10.

1016/0017-9310(86)90190-9

[74] Voigt, W.: Lehrbuch Der Kristallphysik. Vieweg+teubner Verlag, ??? (1928)

[75] Reuss, A.: Berechnung der Fließgrenze von Mischkristallen. Zeitschrift für Angewandte Mathematik und Mechanik **9**(1), 49–58 (1929) https://doi.org/10.1002/zamm.19290090104

[76] Hashin, Z.: The elastic moduli of heterogeneous materials. Journal of Applied Mechanics **29**(1), 143–150 (1962) https://doi.org/10.1115/1.3636446

[77] Akaike, H.: A new look at the statistical model identification. IEEE Transactions on Automatic Control **19**(6), 716–723 (1974) https://doi.org/10.1109/TAC.1974.1100705

[78] Schwarz, G.E.: Estimating the dimension of a model. The Annals of Statistics **6**(2), 461–464 (1978) https://doi.org/10.1214/aos/1176344136

[79] Hannan, E.J., Quinn, B.G.: The determination of the order of an autoregression. Journal of the Royal Statistical Society: Series B (Methodological) **41**(2), 190–195 (1979) https://doi.org/10.1111/j.2517-6161.1979.tb01072.x

[80] Cavaliere, P.: Laser Cladding of Metals. Springer, ??? (2020). https://doi.org/10.1007/978-3-030-53195-9

[81] Aggarwal, A., Pandiyan, V., Leinenbach, C., Leparoux, M.: Investigating laser beam shadowing and powder particle dynamics in directed energy deposition through high-fidelity modelling and high-speed imaging. Additive Manufacturing **91**, 104344 (2024) https://doi.org/10.1016/j.addma.2024.104344

[82] Han, Y., Zhang, X., Liu, H., Xu, M., Gao, G.: Structural design, numerical examination and experimental approach of the multi-powder mixer for directed

energy deposition. Powder Technology **398**, 117144 (2022) https://doi.org/10.1016/j.powtec.2022.117144

[83] Verezub, O., Kálazi, Z., Buza, G., Verezub, N.V., Kaptay, G.: In-situ synthesis of a carbide reinforced steel matrix surface nanocomposite by laser melt injection technology and subsequent heat treatment. Surface and Coatings Technology **203**(20-21), 3049–3057 (2009) https://doi.org/10.1016/j.surfcoat.2009.03.024

[84] Onnes, H.K.: Expression of the equation of state of gases and liquids by means of series. In: Through Measurement to Knowledge, pp. 146–163. Springer, Dordrecht (1991)

[85] Vargaftik, N.B.: Tables on the Thermophysical Properties of Liquids and Gases: in Normal and Dissociated States, p. 758. Hemisphere Publishing Co., ??? (1975)

[86] Dymond, J.H., Marsh, K., Wilhoit, R.C., Wong, K.C.: The Virial Coefficients of Pure Gases and Mixtures. Group IV: Physical Chemistry Subvolumes A and B, 1–328 (2001)

[87] Frenkel, M., Marsh, K.N. (eds.): Virial Coefficients of Pure Gases. Springer, Berlin/Heidelberg (2002)

[88] Reijonen, J., Revuelta, A., Riipinen, T., Ruusuvuori, K., Puukko, P.: On the effect of shielding gas flow on porosity and melt pool geometry in laser powder bed fusion additive manufacturing. Additive Manufacturing **32**, 101030 (2020) https://doi.org/10.1016/j.addma.2019.101030

[89] Fieldhouse, I.B., Hedge, J.C., Lang, J.I.: Measurements of thermal properties. Technical Report WADC-TR-58-274, Wright Air Development Center (1958)

[90] Yamada, N., Okaji, M., Nara, K., Kato, H.: Thermal expansion in stainless steels

at 10-300 K. In: Proc. 4th Asian Thermophysical Properties Conference, vol. 4, pp. 441–444 (1995)

[91] Li, J.J.Z., Johnson, W.L., Rhim, W.-K.: Thermal expansion of liquid Ti-6Al-4V measured by electrostatic levitation. Applied Physics Letters **89**(11), 111913 (2006) https://doi.org/10.1063/1.2349840

[92] Schmon, A., Aziz, K., Pottlacher, G.: Density of liquid Ti-6Al-4V. EPJ Web of Conferences **151**, 04003 (2017) https://doi.org/10.1051/epjconf/201715104003

[93] Solberg, J.M., Hodge, N.E., Puso, M.A., Castonguay, S.T., Ganeriwala, R.K., Ferencz, R.M.: Diablo: A Parallel Implicit Multi-physics Finite Element Code for Engineering Analysis User Manual. Lawrence Livermore National Laboratory (2018)

[94] Ganeriwala, R.K., Strantza, M., King, W.E., Clausen, B., Phan, T.Q., Levine, L.E., Brown, D.W., Hodge, N.E.: Evaluation of a thermomechanical model for prediction of residual stress during laser powder bed fusion of Ti-6Al-4V. Additive Manufacturing **27**, 489–502 (2019) https://doi.org/10.1016/j.addma.2019.03.034

[95] Abdullaev, R.N., Khairulin, R.A., Stankus, S.V., Kozlovskii, Y.M.: Density and volumetric expansion of the Inconel 718 alloy in solid and liquid states. Thermophysics and Aeromechanics **26**(5), 785–788 (2019) https://doi.org/10.1134/S0869864319050160

[96] Blumm, J., Henderson, J.: Measurement of the volumetric expansion and bulk density of metals in the solid and molten regions. High Temperatures-High Pressures **32**(1), 109–113 (2000) https://doi.org/10.1068/htwu520

[97] Wang, H.P., Zheng, C.H., Zou, P.F., Yang, S.J., Hu, L., Wei, B.: Density determination and simulation of Inconel 718 alloy at normal and metastable liquid states. Journal of Materials Science & Technology **34**(3), 436–439 (2018) https://doi.org/10.1016/j.jmst.2017.10.014

[98] Richardson, M.J., Hayes, D., Day, A.P., Mills, K.C.: NPL Report on DSC. Technical report, National Physical Laboratory, Teddington, UK (1996)

[99] Haas, J.L., Fisher, J.R.: Simultaneous evaluation and correlation of thermodynamic data. American Journal of Science **276**, 525–545 (1976) https://doi.org/10.2475/ajs.276.4.525

[100] Fei, Y., Saxena, S.K.: An equation for the heat capacity of solids. Geochimica et Cosmochimica Acta **51**, 251–254 (1987) https://doi.org/10.1016/0016-7037(87)90236-5

[101] Mills, K.C.: Heat capacity of slags. In: (VDEh), V.D.E. (ed.) Slag Atlas, 2nd edn., pp. 9–43. Verlag Stahleisen, Düsseldorf (1995)

[102] Kubaschewski, O., Alcock, C.B., Spencer, P.J.: Materials Thermochemistry, 6th edn. Pergamon Press, ??? (1993)

[103] Barin, I.: Thermochemical Data of Pure Substances, 3rd edn. VCH Publishers, ??? (1995). https://doi.org/10.1002/9783527619825

[104] Dinsdale, A.T.: SGTE data for pure elements. Calphad **15**(4), 317–425 (1991) https://doi.org/10.1016/0364-5916(91)90030-N

[105] Douglas, T., Victor, A.: Enthalpy and specific heat of corrosion-resistant alloys at high temperatures. Technical Report WADC-TR-57-374, U.S. Air Force (1957)

[106] Douglas, T., Victor, A.: Enthalpy and specific heat of 9 corrosion-resistant alloys

at high temperatures. Journal of Research of the National Bureau of Standards, Section C **65C**, 65 (1961) https://doi.org/10.6028/jres.065C.008

[107] Lucks, C.F., Deem, H.W.: Thermal properties of metals. Technical Report Spec. Tech. Publ. 227, ASTM (1958)

[108] Lucks, C.F.: Thermal properties of metals. Technical Report AF-TR-6145, U.S. Air Force (1954)

[109] Redmond, R.F., Lanes, J.: Thermal properties of metals. Technical Report ORNL-1342, USAEC (1952)

[110] Cezairliyan, A., McClure, J.L., Taylor, R.: Thermophysical Measurements on 90Ti-6Al-4V Alloy Above 1450 K. Journal of Research of the National Bureau of Standards - A. Physics and Chemistry **81A**(2-3), 251–256 (1977) https://doi.org/10.6028/jres.081A.024

[111] Ho, C.-Y., Chu, T.: Thermal Conductivity and Electrical Resistivity of Eight Selected AISI Stainless Steels. Thermal Conductivity **15**, 53 (1977) https://doi.org/10.1007/978-1-4615-9083-5_12

[112] Zhou, Q., Wang, Y., Choi, S.-K., Cao, L., Gao, Z.: Robust optimization for reducing welding-induced angular distortion in fiber laser keyhole welding under process parameter uncertainty. Applied Thermal Engineering **129**, 893–906 (2017) https://doi.org/10.1016/j.applthermaleng.2017.10.081

[113] Ganeriwala, R.K., Strantza, M., King, W.E., Clausen, B., Phan, T.Q., Levine, L.E., Brown, D.W., Hodge, N.E.: Evaluation of a thermomechanical model for prediction of residual stress during laser powder bed fusion of Ti-6Al-4V. Additive Manufacturing **27**, 489–502 (2019) https://doi.org/10.1016/j.addma.2019.03.034

[114] Musaeva, Z., Peletskii, V.: Experimental Investigation of the Thermal Conductivity of VT6 Alloy. High Temperature **40**, 838–842 (2002) https://doi.org/10.1023/A:1021421132086

[115] Anderson, M., Patwa, R., Shin, Y.C.: Laser-assisted machining of Inconel 718 with an economic analysis. International Journal of Machine Tools and Manufacture **46**(14), 1879–1891 (2006) https://doi.org/10.1016/j.ijmachtools.2005.11.005

[116] Hust, J.G., Weitzel, D.H., Powell, R.L.: Thermal conductivity, electrical resistivity, and thermopower of aerospace alloys from 4 to 300 K. Journal of Research of the National Bureau of Standards Section A: Physics and Chemistry **75A**(4), 269–277 (1971) https://doi.org/10.6028/jres.075a.025

[117] Machno, M.: Investigation of the Machinability of the Inconel 718 Superalloy during the Electrical Discharge Drilling Process. Materials **13**(15), 3392 (2020) https://doi.org/10.3390/ma13153392

[118] McElroy, D.L., Williams, R.K., Moore, J.P., Graves, R.S., Weaver, F.J.: The physical properties of Inconel alloy 718 from 300 to 1000 K. In: Thermal Conductivity 15, pp. 149–151. Plenum Press, New York (1978). https://doi.org/10.1007/978-1-4615-9083-5_18

[119] Lykov, A.: Theory of Thermal Conductivity, p. 599. Vysshaya shkola, Moscow (1967)

[120] Ofuchi, K., Kunii, D.: Heat-transfer Characteristics of Packed Beds with Stagnant Fluids. International Journal of Heat and Mass Transfer **8**, 749–757 (1964)

[121] Nozad, I.: An Experimental and Theoretical Study of Heat Conduction in two-

and three-phase systems. PhD thesis, University of California, Davis (1983)

[122] Nozad, I., Carbonell, R.G., Whitaker, S.: Heat Conduction in MultiPhase Systems I: Theory and Experiments for two-phase systems. Chemical Engineering Science **40**, 843–855 (1985)

[123] Nikolenko, A.N., Koval'chenko, M.S.: Analysis of the random packing of identical particles - III. Tapping of spherical powders. Soviet Powder Metallurgy and Metal Ceramics **25**(1), 24–26 (1986) https://doi.org/10.1007/BF00843011

[124] Cumberland, D.J., Crawford, R.J., Sprevak, D.: A statistical model for the random packing of real powder particles. European Polymer Journal **25**(11), 1173–1182 (1989) https://doi.org/10.1016/0014-3057(89)90176-6

[125] Milošević, N., Aleksić, I.: Thermophysical properties of solid phase Ti-6Al-4V alloy over a wide temperature range. International Journal of Materials Research **103**(6), 707–714 (2012) https://doi.org/10.3139/146.110678

[126] Sweet, J.N., Roth, E.P., Moss, M.: Thermal conductivity of Inconel 718 and 304 stainless steel. International Journal of Thermophysics **8**(5), 593–606 (1987) https://doi.org/10.1007/BF00503645

[127] Kaschnitz, E., Kaschnitz, H., Schleutker, T., Gülhan, A., Bonvoisin, B.: Electrical resistivity measured by millisecond pulse-heating in comparison to thermal conductivity of the stainless steel AISI 316L at elevated temperature. High Temperatures-High Pressures **46**(4-5), 353–365 (2017)

[128] Deem, H.W., Wood, W.D., Lucks, C.F.: The relationship between electrical and thermal conductivities of titanium alloys. Transactions of the Metallurgical Society of AIME **212**, 520 (1958)

[129] Grant, D.M., Wood, J.V.: Surface tension of electromagnetically levitated 316L stainless steel with sulphur and silicon. Powder Metallurgy **35**(1), 43–46 (1992) https://doi.org/10.1179/pom.1992.35.1.43

[130] Mills, K.C., Keene, B.J.: Factors affecting variable weld penetration. International Materials Reviews **35**(1), 185–216 (1990) https://doi.org/10.1179/095066090790323966

[131] Bayat, M., Nadimpalli, V.K., Pedersen, D.B., Hattel, J.H.: A fundamental investigation of thermo-capillarity in laser powder bed fusion of metals and alloys. International Journal of Heat and Mass Transfer **166**, 120766 (2021) https://doi.org/10.1016/j.ijheatmasstransfer.2020.120766

[132] Mckay, D.S., Heiken, G., Basu, A., Blanford, G., Simon, S., Reedy, R., French, B.M., Papike, J.: The lunar regolith. In: Lunar Sourcebook: A User's Guide to the Moon, p. 296. Cambridge University Press, ??? (1991)

[133] Rhodes, J., Blanchard, D.: Apollo 11 breccias and soils - aluminous mare basalts or multi-component mixtures. In: Lunar and Planetary Science Conference, pp. 607–620. Pergamon Press, Houston (1981). https://articles.adsabs.harvard.edu//full/1982LPSC...12..607R/0000608.000.html

[134] Haskin, L., Helmke, P., Blanchard, D., Jacobs, J., Telander, K.: Major and trace element abundances in samples from the lunar highlands. In: Proceedings of the Fourth Lunar Science Conference, Wisconsin, pp. 1275–1296 (1973). https://articles.adsabs.harvard.edu//full/1973LPSC....4.1275H/0001279.000.html

[135] Mueller, R.P., Sibille, L., Hintze, P.E., Lippitt, T.C., Mantovani, J.G., Nugent, M.W., Townsend, I.I.: Additive construction using basalt regolith fines. In: Earth

and Space 2014 - Engineering for Extreme Environments. 14th Biennial International Conference on Engineering, Science, Construction and Operations in Challenging Environments, pp. 394–403. American Society of Civil Engineers, ??? (2015). http://www.contourcrafting.org

[136] Chao, E.C.T., Boreman, J.A., Minkin, J.A., James, O.B., Desborough, G.A.: Lunar glasses of impact origin: physical and chemical characteristics and geologic implications. Journal of Geophysical Research **75**(35), 7445–7479 (1970) https://doi.org/10.1029/JB075i035p07445

[137] Yang, J., Schlenger, L.M., Nasab, M.H., Van Petegem, S., Marone, F., Logé, R.E., Leinenbach, C.: Experimental quantification of inward Marangoni convection and its impact on keyhole threshold in laser powder bed fusion of stainless steel. Additive Manufacturing **84**, 104092 (2024) https://doi.org/10.1016/j.addma.2024.104092

[138] Leung, C.L.A., Marussi, S., Towrie, M., Atwood, R.C., Withers, P.J., Lee, P.D.: The effect of powder oxidation on defect formation in laser additive manufacturing. Acta Materialia **166**, 294–305 (2019) https://doi.org/10.1016/j.actamat.2018.12.027

[139] Leung, C.L.A., Marussi, S., Towrie, M., Garcia, J.d.V., Atwood, R.C., Bodey, A.J., Jones, J.R., Withers, P.J., Lee, P.D.: Laser-matter interactions in additive manufacturing of stainless steel SS316L and 13-93 bioactive glass revealed by in situ X-ray imaging. Additive Manufacturing **24**, 647–657 (2018) https://doi.org/10.1016/j.addma.2018.08.025

[140] Aucott, L., Dong, H., Mirihanage, W., *et al.*: Revealing internal flow behaviour in arc welding and additive manufacturing of metals. Nature Communications **9**, 5414 (2018) https://doi.org/10.1038/s41467-018-07900-9

[141] Guo, Q., Qu, M., Escano, L.I., Hojjatzadeh, S.M.H., Young, Z., Fezzaa, K., Chen, L.: Revealing melt flow instabilities in laser powder bed fusion additive manufacturing of aluminum alloy via in-situ high-speed X-ray imaging. International Journal of Machine Tools and Manufacture **175**, 103861 (2022) https://doi.org/10.1016/j.ijmachtools.2022.103861

[142] J., V.: Surface tension of steel at high temperatures. SN Applied Sciences **5**, 237 (2023) https://doi.org/10.1007/s42452-023-05456-y

[143] Egry, I., Brillo, Holland-Moritz, D., Plevachuk, Y.: The surface tension of liquid aluminium-based alloys. Materials Science and Engineering **495**, 14–18 (2008) https://doi.org/10.1016/j.msea.2007.07.104

[144] Kang, Y., Jung, I.H.: Model for Surface Tension of Pure Liquid Metals: Revisit to Iida's Model. Metallurgical and Materials Transactions B **55**, 3698–3710 (2024) https://doi.org/10.1007/s11663-024-03209-9

[145] Qiao, Z., Yan, L., Cao, Z., Xie, Y.: Surface tension prediction of high-temperature melts. Journal of Alloys and Compounds **325**(1–2), 180–189 (2001) https://doi.org/10.1016/S0925-8388(01)01362-7

[146] Chia, H.Y., Wang, L., Yan, W.: Influence of oxygen content on melt pool dynamics in metal additive manufacturing: High-fidelity modeling with experimental validation. Acta Materialia **249**, 118824 (2023) https://doi.org/10.1016/j.actamat.2023.118824

[147] Tang, C., Le, K.Q., Wong, C.H.: Physics of humping formation in laser powder bed fusion. International Journal of Heat and Mass Transfer **149**, 119172 (2020) https://doi.org/10.1016/j.ijheatmasstransfer.2019.119172

[148] Small, W.M., Sahoo, P., Li, K.: Prediction of surface tension in molten Fe-O-S system. Scripta Metallurgica et Materialia **24**(6), 1155–1158 (1990) https://doi.org/10.1016/0956-716X(90)90316-9

[149] Lomaev, S.L., Gordeev, G.A., Timirgazin, M.A., Fattalova, D.R., Krivilyov, M.D.: Interplay between temperature oscillations and melt-pool dynamics in 3D-manufacturing techniques. Physical Review Applied **25**, 034012 (2026) https://doi.org/10.1103/sj3d-ghlg

[150] May, J., Janthur, F., Kreie, L., Müller, M., Seffer, S., Schwarz, N., Hermsdorf, J., Hassel, T., Kaierle, S., Overmeyer, L.: Surface tension measurement of ti-6al-4v by falling droplet method in oxygen-free atmosphere. Advanced Engineering Materials **28**(12) (2026) https://doi.org/10.1002/adem.202502957

[151] Battezzati, L., Greer, A.L.: The viscosity of liquid metals and alloys. Acta Metallurgica **37**, 1791–1802 (1989) https://doi.org/10.1016/0001-6160(89)90064-3

[152] Hirai, M., Takebayashi, K., Yoshikawa, Y., Yamaguchi, R.: Apparent Viscosity of Al-10 mass%Cu Semi-solid Alloys. ISIJ International **33**, 405–412 (1993) https://doi.org/10.2355/isijinternational.33.405

[153] Herlach, D.M., Cochrane, R.F., Egry, I., Fecht, H.J., Greer, A.L.: Containerless processing in the study of metallic melts and their solidification. International Materials Reviews **38**(6), 273–347 (1993) https://doi.org/10.1179/095066093790326267

[154] Sterkhova, I.V., Kamaeva, L.V., Lad'yanov, V.I.: Viscosity of the eutectic Fe85-xCr15Cx (x=10–17) melts. Physics and Chemistry of Liquids **58**(5), 559–565 (2020) https://doi.org/10.1080/00319104.2019.1616194

[155] Sterkhova, I.V., Kamaeva, L.V., Lad'yanov, V.I., Chtchelkatchev, N.M.: Role

of Ta and Nb alloying elements on the viscosity of Fe-B-Si melts. Journal of Molecular Liquids **323**, 114636 (2021) https://doi.org/10.1016/j.molliq.2020.114636

[156] Flemings, M.C.: Behavior of metal alloys in the semisolid state. Metallurgical Transactions A **22**(5), 957–981 (1991) https://doi.org/10.1007/BF02661090

[157] Kokubo, H., Nishi, T., Ohta, H., Yamano, H.: Viscosity Measurement of Nickel and Stainless Steel. Journal of the Japan Institute of Metals and Materials **82**, 400–402 (2018) https://doi.org/10.2320/jinstmet.JAW201812

[158] Wachtman, J.B.J., Tefft, W.E., Lam, D.G.J., Apstein, C.S.: Exponential temperature dependence of Young's modulus for several oxides. Physical Review **122**, 1754–1759 (1961) https://doi.org/10.1103/PhysRev.122.1754

[159] Anderson, O.L.: Derivation of Wachtman's equation for the temperature dependence of elastic moduli of oxide compounds. Physical Review **144**, 553–557 (1966) https://doi.org/10.1103/PhysRev.144.553

[160] Li, W., Wang, R., Liu, D., Deng, F.: A model of temperature-dependent Young's modulus for ultrahigh temperature ceramics. Physics Research International (2011)

[161] Davis, J.R.: Stainless Steels. ASM specialty handbook. ASM International, ??? (1994)

[162] Elevated temperature physical properties of stainless steels. https://bssa.org.uk/bssa_articles/elevated-temperature-physical-properties-of-stainless-steels/. Accessed 26-06-2025

[163] Scheuerlein, C., Lackner, F., Savary, F., Rehmer, B., Finn, M., Meyer, C.:

Thermomechanical Behavior of the HL-LHC 11 Tesla Nb3Sn Magnet Coil Constituents During Reaction Heat Treatment. IEEE Transactions on Applied Superconductivity **28**(3), 1–6 (2018) https://doi.org/10.1109/tasc.2018.2792485

[164] Rangaswamy, P.: High Temperature Stress Assessment in SCS-6/Ti-6Al-4V Composite Using Neutron Diffraction and Finite Element Modeling. (2000). Los Alamos National Lab. https://www.osti.gov/biblio/766370

[165] Julien, R., Velay, V., Vidal, V., Dahan, Y., Forestier, R., Rézaï-Aria, F.: Characterization and modeling of forged Ti-6Al-4V Titanium alloy with microstructural considerations during quenching process. International Journal of Mechanical Sciences **142-143**, 456–467 (2018) https://doi.org/10.1016/j.ijmecsci.2018.05.023

[166] ATI: ATI 718 Alloy Technical Data Sheet. Technical report (2017). https://www.atimaterials.com/Products/Documents/datasheets/nickel-cobalt/nickel-based/ati_718_ludlum_version_tds_en_v1.pdf

[167] Chen, S.R., Gray, G.T.: The constitutive behavior of tantalum and tantalum-tungsten alloys. Metallurgical and Materials Transactions A **27**, 2994–3006 (1996) https://doi.org/10.1007/BF02663852

[168] Goto, D.M., Bingert, J.F., Reed, W.R., Garrett, R.K.: Anisotropy corrected MTS constitutive strength modeling in HY-100 steel. Scripta Materialia **42**, 1129–1134 (2000) https://doi.org/10.1016/S1359-6462(00)00374-9

[169] Byun, T.S., Lach, T.G.: Mechanical properties of 304L and 316L austenitic stainless steels after thermal aging for 1500 hours. Technical Report PNNL-25854, Pacific Northwest National Laboratory (2016)

[170] Gerstler, W.D., Barua, A., Huang, S., Erno, D.J., Wang, Y., Ju, S., Thiagarajan,

N.: Binder Jet Additive Manufacturing Process and Material Characterization for High Temperature Heat Exchangers Used in Concentrated Solar Power Applications. Metals **13**(3), 617 (2023) https://doi.org/10.3390/met13030617

[171] Alleima: Sanmac® 316/316L – Solid Bar. Alleima technical center, material datasheets. Accessed: 2025-06-27 (2025). https://www.alleima.com/en/technical-center/material-datasheets/bar-and-hollow-bar/bar/sanmac-316316l/

[172] Ivanov, S., Gushchina, M.O., Artinov, A., Khomutov, M., Zemlyakov, E.: Effect of Elevated Temperatures on the Mechanical Properties of a Direct Laser Deposited Ti-6Al-4V. Materials **14**, 6432 (2021) https://doi.org/10.3390/ma14216432

[173] Babentsova, L.P., Antsiferova, I.V.: The mechanical properties of the IN718 alloy under static and cyclic deformation. Modern High Technologies **6**, 14–19 (2019) https://doi.org/10.17513/snt.37542

[174] Special Metals Corporation: INCONEL alloy 718. Technical report (2007). https://www.specialmetals.com/documents/technical-bulletins/inconel/inconel-alloy-718.pdf

[175] Bibus Metals: Inconel 718 Technical Data Sheet. Technical report (2020). https://www.bibusmetals.ru/fileadmin/materials/PDF/catalogs_new_2013/nikel/INCONEL__Alloy_718_RU_EN.pdf

[176] Titanium. https://www.kobelco.co.jp/english/titan. Accessed 27-06-2025

**Table 12**: Results of determining the optimal order of polynomial decomposition for 316L steel, Ti–6Al–4V, and Inconel 718 alloys.

| **Property** | **Optimal degree** | **AIC** | **BIC** | **HQC** | **Polynomial fit** |
|---|---|---|---|---|---|
| *SS316L* | | | | | |
| Young's modulus | $[0; 2]$ | 1960.6 | 1965.9 | 1962.6 | $2.45 \cdot 10^{11} - 1.30 \cdot 10^{8}T + 2.912 \cdot 10^{4}T^{2}$ |
| Shear modulus | $[0; 2]$ | 941.45 | 942.78 | 944.72 | $9.27 \cdot 10^{10} - 5.82 \cdot 10^{7}T + 1.91 \cdot 10^{4}T^{2}$ |
| Poisson's ratio | $[0; 1]$ | $-117.47$ | $-116.50$ | $-117.83$ | $2.73 \cdot 10^{-1} + 4.87 \cdot 10^{-5}T$ |
| Yield strength | $[-1; 0]$ | 615.05 | 616.94 | 615.37 | $4.92 \cdot 10^{10}T^{-1} + 6.45 \cdot 10^{7}$ |
| *Ti–6Al–4V* | | | | | |
| Young's modulus | $[0; 1]^{*\text{BIC}}$ | 2390.6 | 2394.5 | 2392.1 | |
| | $[0; 3]^{*\text{HQC}}$ | 2387.2 | 2395.0 | 2390.2 | $1.38 \cdot 10^{11} - 6.73 \cdot 10^{7}T$ |
| | $[0; 4]^{*\text{AIC}}$ | 2387.1 | 2396.8 | 2390.8 | |
| Shear modulus** | $[-3; 3]$ | $-104.74$ | $-105.12$ | $-109.42$ | $4.94 \cdot 10^{10} - 2.045 \cdot 10^{7}T$ |
| Poisson's ratio*** | $[-3; 3]$ | $-438.89$ | $-439.27$ | $-443.57$ | $0.326 - 5.4 \cdot 10^{-5}T + 1.397 \cdot 10^{-7}T^{2} - 3.39 \cdot 10^{-11}T^{3}$ |
| Yield strength**** | $[0; 1]^{*\text{BIC}}$ | 632.01 | 633.68 | 632.18 | |
| | $[0; 4]^{*\text{AIC}}$ | 637.22 | 635.93 | 632.18 | $1.32 \cdot 10^{9} - 1.12 \cdot 10^{6}T$ |
| | $[0; 4]^{*\text{HQC}}$ | 637.22 | 635.93 | 632.18 | |
| *Inconel 718* | | | | | |
| Young's modulus | $[0; 2]$ | 1030.18 | 1032.32 | 1029.77 | $2.0784 \cdot 10^{11} - 1.9704 \cdot 10^{7}T - 2.9188 \cdot 10^{4}T^{2}$ |
| Shear modulus | $[0; 1]$ | 1592.75 | 1595.75 | 1593.61 | $8.47 \cdot 10^{10} - 2.344 \cdot 10^{7}T$ |
| Poisson's ratio | $[0; 2]$ | $-108.33$ | $-108.82$ | $-110.91$ | $0.33 - 1.65 \cdot 10^{-4}T + 1.37 \cdot 10^{-7}T^{2}$ |
| Yield strength | $[0; 3]$ | 3648.41 | 3658.27 | 3652.14 | $1.4065 \cdot 10^{9} - 2.0429 \cdot 10^{6}T + 3.4921 \cdot 10^{3}T^{2} - 2.0021T^{3}$ |

* – Because of conflicting results obtained from various criteria, the final choice was made based on visual analysis. The linear model shows the best agreement with the experimental data and was therefore adopted as the primary one.

**,**** – Although formal criteria deliver the optimality of higher-degree polynomials (from $-3$ to 3 and from 0 to 4), visual analysis of their fitted curves revealed excessive complexity and non-physical behavior. Thus, a simple and interpretable linear model was chosen for the correct representation of the data.

*** – The analysis showed that although formal optimality criteria were achieved for polynomials in the range $[-3; 3]$, visual assessment of their adequacy revealed several drawbacks. As a compromise between criterion-based accuracy and clarity of representation, a limited polynomial range from 0 to 3 was selected.

**Table A1**: Thermophysical properties of SS316L stainless steel in the solid state versus temperature.

| $T$ (K) | $\rho$ (kg m$^{-3}$) | $k$ (W m$^{-1}$ K$^{-1}$) | $\rho_{\mathbf{el}}$ ($\mu\Omega$ m) | $c_p$ (J kg$^{-1}$ K$^{-1}$) | $\Delta H$ (J g$^{-1}$) |
|---|---|---|---|---|---|
| 273 | 7966.19 | 13.5368 | 0.700735 | 456.300 | – |
| 323 | 7943.99 | 14.3223 | 0.777330 | 471.186 | – |
| 373 | 7921.59 | 15.1078 | 0.841982 | 484.780 | 5.225 |
| 423 | 7898.99 | 15.8933 | 0.896759 | 497.367 | 43.583 |
| 473 | 7876.20 | 16.6788 | 0.943467 | 509.145 | 79.283 |
| 523 | 7853.22 | 17.4643 | 0.983667 | 520.250 | 112.804 |
| 573 | 7830.04 | 18.2498 | 1.018690 | 530.788 | 144.581 |
| 623 | 7806.67 | 19.0353 | 1.049660 | 540.836 | 175.010 |
| 673 | 7783.10 | 19.8208 | 1.077500 | 550.457 | 204.445 |
| 723 | 7759.33 | 20.6063 | 1.102970 | 559.702 | 233.199 |
| 773 | 7735.38 | 21.3918 | 1.126630 | 568.611 | 261.545 |
| 823 | 7711.22 | 22.1773 | 1.148950 | 577.219 | 289.713 |
| 873 | 7686.88 | 22.9628 | 1.170230 | 585.554 | 317.895 |
| 923 | 7662.34 | 23.7483 | 1.190670 | 593.641 | 346.240 |
| 973 | 7637.60 | 24.5338 | 1.210390 | 601.500 | 374.857 |
| 1023 | 7612.67 | 25.3193 | 1.229430 | 609.150 | 403.815 |
| 1073 | 7587.54 | 26.1048 | 1.247750 | 616.607 | 433.141 |
| 1123 | 7562.22 | 26.8903 | 1.265280 | 623.884 | 462.825 |
| 1173 | 7536.71 | 27.6758 | 1.281940 | 630.994 | 492.812 |
| 1223 | 7511.00 | 28.4613 | 1.297610 | 637.948 | 523.009 |
| 1273 | 7485.09 | 29.2468 | 1.312190 | 644.756 | 553.284 |
| 1323 | 7458.99 | 30.0323 | 1.325610 | 651.426 | 583.464 |
| 1373 | 7432.70 | 30.8178 | 1.337840 | 657.967 | 613.334 |
| 1423 | 7406.21 | 31.6033 | 1.348900 | 664.386 | 642.641 |
| 1473 | 7379.53 | 32.3888 | 1.358900 | 670.690 | 671.093 |
| 1523 | 7352.65 | 33.1743 | 1.368010 | 676.884 | 698.356 |
| 1573 | 7325.57 | 33.9598 | 1.376550 | 682.974 | 724.056 |
| 1623 | 7298.31 | 34.7453 | 1.384930 | 688.965 | 747.782 |
| 1673 | 7270.84 | 35.5308 | 1.393720 | 694.862 | 769.081 |

**Table A2**: Thermophysical properties of SS316L stainless steel in the liquid state and melting range versus temperature.

| $T$ (K) | $\rho$ (kg m$^{-3}$) | $k$ (W m$^{-1}$ K$^{-1}$) | $\rho_{\mathbf{el}}$ ($\mu\Omega$ m) | $c_p$ (J kg$^{-1}$ K$^{-1}$) | $\Delta H$ (J g$^{-1}$) | $\gamma$ (N m$^{-1}$) | $\mu$ (Pa·s) |
|---|---|---|---|---|---|---|---|
| 1679 | 7267.54 | 35.6251 | 1.394840 | 695.563 | 771.451 | – | 302.427000 |
| 1682 | 7239.10 | 35.1547 | 1.400180 | 708.880 | 793.068 | – | 299.556000 |
| 1688 | 7182.20 | 34.2157 | 1.412530 | 714.304 | 841.244 | – | 0.027311 |
| 1691 | 7153.76 | 33.7462 | 1.418700 | 717.016 | 865.332 | – | 0.016374 |
| 1694 | 7125.31 | 33.2767 | 1.424880 | 719.728 | 889.421 | – | 0.012266 |
| 1697 | 7096.86 | 32.8072 | 1.431060 | 722.440 | 913.509 | – | 0.010218 |
| 1700 | 7068.41 | 32.3377 | 1.437230 | 725.152 | 937.597 | – | 0.009061 |
| 1703 | 7039.97 | 31.8682 | 1.443410 | 727.864 | 961.685 | – | 0.008368 |
| 1706 | 7011.52 | 31.3987 | 1.449590 | 730.576 | 985.773 | – | 0.007945 |
| 1709 | 6983.07 | 30.9292 | 1.455760 | 733.288 | 1009.860 | – | 0.007693 |
| 1712 | 6954.62 | 30.4597 | 1.461940 | 736.000 | 1033.950 | – | 0.007556 |
| 1723 | 6946.66 | 30.6346 | 1.472970 | 736.000 | 1062.920 | 1.674 | 0.007303 |
| 1773 | 6910.51 | 31.4253 | 1.483730 | – | 1141.800 | 1.694 | 0.006305 |
| 1823 | 6874.36 | 32.2160 | 1.494360 | – | 1204.490 | 1.714 | 0.005487 |
| 1873 | 6838.22 | 33.0068 | 1.504870 | – | 1256.040 | 1.734 | 0.004811 |
| 1923 | 6802.07 | 33.7975 | 1.515250 | – | 1300.460 | 1.754 | 0.004247 |
| 1973 | 6765.92 | 34.5882 | 1.525520 | – | 1340.850 | 1.774 | 0.003773 |
| 2023 | 6729.78 | 35.3789 | 1.535680 | – | 1379.540 | 1.794 | 0.003372 |
| 2073 | 6693.63 | 36.1697 | 1.545740 | – | 1418.110 | 1.814 | 0.003029 |
| 2123 | 6657.48 | 36.9604 | 1.555690 | – | 1457.550 | 1.834 | 0.002735 |
| 2173 | 6621.34 | 37.7511 | 1.565560 | – | 1498.330 | 1.854 | 0.002482 |
| 2223 | 6585.19 | 38.5418 | 1.575330 | – | 1540.520 | 1.874 | 0.002261 |
| 2273 | 6549.04 | 39.3326 | 1.585010 | – | 1583.870 | 1.894 | 0.002069 |
| 2323 | 6512.90 | 40.1233 | 1.594610 | – | 1627.930 | 1.914 | 0.001900 |
| 2373 | 6476.75 | 40.9140 | 1.604130 | – | 1672.120 | 1.934 | 0.001752 |
| 2423 | 6440.60 | 41.7047 | 1.613580 | – | 1715.870 | 1.954 | 0.001620 |
| 2473 | 6404.45 | 42.4955 | 1.622950 | – | 1758.670 | 1.974 | 0.001503 |
| 2523 | 6368.31 | 43.2862 | 1.632260 | – | 1800.210 | 1.994 | 0.001399 |
| 2573 | 6332.16 | 44.0769 | 1.641490 | – | 1840.470 | 2.014 | 0.001305 |
| 2623 | 6296.01 | 44.8676 | 1.650670 | – | 1879.800 | 2.034 | 0.001221 |
| 2673 | 6259.87 | 45.6584 | 1.659780 | – | 1919.040 | 2.054 | 0.001146 |
| 2723 | 6223.72 | 46.4491 | 1.668840 | – | 1959.630 | 2.074 | 0.001077 |
| 2773 | 6187.57 | 47.2398 | 1.677840 | – | 2003.670 | 2.094 | 0.001015 |
| 2823 | 6151.43 | 48.0305 | 1.686790 | – | 2054.050 | 2.114 | 0.000958 |
| 2873 | 6115.28 | 48.8213 | 1.695690 | – | 2114.550 | 2.134 | 0.000907 |
| 2923 | 6079.13 | 49.6120 | 1.704540 | – | 2189.910 | 2.154 | 0.000860 |
| 2973 | 6042.99 | 50.4027 | 1.713340 | – | 2285.960 | 2.174 | 0.000816 |
| 3023 | 6006.84 | 51.1934 | 1.722100 | – | 2409.730 | 2.194 | 0.000776 |

**Table A3**: Thermophysical properties of Ti–6Al–4V alloy in the solid state versus temperature.

| $T$ (K) | $\rho$ (kg m$^{-3}$) | $k$ (W m$^{-1}$ K$^{-1}$) | $\rho_{\mathbf{el}}$ ($\mu\Omega$ m) | $c_p$ (J kg$^{-1}$ K$^{-1}$) | $\Delta H$ (J g$^{-1}$) |
|---|---|---|---|---|---|
| 273 | 4423.85 | 5.25026 | 1.726180 | 530.587 | – |
| 323 | 4416.15 | 5.90443 | 1.762270 | 550.365 | 181.329 |
| 373 | 4408.45 | 6.55861 | 1.793820 | 568.258 | 208.228 |
| 423 | 4400.75 | 7.21278 | 1.821070 | 584.390 | 236.373 |
| 473 | 4393.05 | 7.86696 | 1.844250 | 598.884 | 266.429 |
| 523 | 4385.35 | 8.52113 | 1.863580 | 611.861 | 298.854 |
| 573 | 4377.65 | 9.17531 | 1.879290 | 623.445 | 333.922 |
| 623 | 4369.95 | 9.82948 | 1.891620 | 633.759 | 371.737 |
| 673 | 4362.25 | 10.48370 | 1.900780 | 642.924 | 412.250 |
| 723 | 4354.55 | 11.13780 | 1.907020 | 651.064 | 455.283 |
| 773 | 4346.85 | 11.79200 | 1.910550 | 658.301 | 500.537 |
| 823 | 4339.15 | 12.44620 | 1.911600 | 664.448 | 547.621 |
| 873 | 4331.45 | 13.10040 | 1.910410 | 671.258 | 596.059 |
| 923 | 4323.75 | 13.75450 | 1.907210 | 683.957 | 645.318 |
| 973 | 4316.05 | 14.40870 | 1.902210 | 705.811 | 694.817 |
| 1023 | 4308.35 | 15.06290 | 1.895650 | 740.089 | 743.950 |
| 1073 | 4300.65 | 15.71710 | 1.887770 | 790.059 | 792.103 |
| 1123 | 4292.95 | 16.37120 | 1.878780 | 858.987 | 838.671 |
| 1173 | 4285.25 | 17.02540 | 1.868910 | 954.641 | 883.074 |
| 1223 | 4277.55 | 17.67960 | 1.858400 | 1120.080 | 924.780 |
| 1273 | 4269.85 | 18.33380 | 1.847470 | 707.995 | 963.319 |
| 1323 | 4262.15 | 18.98790 | 1.836350 | 713.395 | 998.300 |
| 1373 | 4254.45 | 19.64210 | 1.825260 | 719.364 | 1029.430 |
| 1423 | 4246.75 | 20.29630 | 1.814450 | 726.025 | 1056.540 |
| 1473 | 4239.05 | 20.95050 | 1.804140 | 733.499 | 1079.580 |
| 1523 | 4231.35 | 21.60460 | 1.794540 | 741.910 | 1098.660 |
| 1573 | 4223.65 | 22.25880 | 1.785910 | 751.381 | 1114.070 |
| 1623 | 4215.95 | 22.91300 | 1.778450 | 762.033 | 1126.270 |
| 1673 | 4208.25 | 23.56720 | 1.772400 | 773.990 | 1135.940 |
| 1723 | 4200.55 | 24.22130 | 1.767990 | 787.375 | 1143.960 |
| 1773 | 4192.85 | 24.87550 | 1.765450 | 802.309 | 1151.480 |
| 1823 | 4185.15 | 25.52970 | 1.765010 | 818.916 | 1159.900 |
| 1873 | 4177.45 | 26.18390 | 1.766890 | 837.318 | 1170.880 |

**Table A4**: Thermophysical properties of Ti–6Al–4V alloy in the liquid state and melting range versus temperature.

| $T$ (K) | $\rho$ (kg m$^{-3}$) | $k$ (W m$^{-1}$ K$^{-1}$) | $\rho_{\mathbf{el}}$ ($\mu\Omega$ m) | $c_p$ (J kg$^{-1}$ K$^{-1}$) | $\Delta H$ (J g$^{-1}$) | $\gamma$ (N m$^{-1}$) | $\mu$ (Pa·s) |
|---|---|---|---|---|---|---|---|
| 1878 | 4176.68 | 26.2493 | 1.767210 | 839.262 | 1172.190 | – | 406.417000 |
| 1881 | 4170.40 | 26.4058 | 1.755270 | 840.437 | 1192.840 | – | 404.305000 |
| 1884 | 4164.12 | 26.5625 | 1.746540 | 841.620 | 1213.900 | – | 402.211000 |
| 1887 | 4157.85 | 26.7191 | 1.737810 | 842.809 | 1234.960 | – | 400.134000 |
| 1890 | 4151.57 | 26.8757 | 1.729080 | 844.006 | 1256.020 | – | 398.075000 |
| 1893 | 4145.29 | 27.0323 | 1.720350 | 845.209 | 1277.090 | – | 396.033000 |
| 1896 | 4139.02 | 27.1890 | 1.711620 | 846.420 | 1298.150 | – | 394.008000 |
| 1899 | 4132.74 | 27.3456 | 1.702880 | 847.638 | 1319.210 | – | 391.999000 |
| 1902 | 4126.46 | 27.5022 | 1.694150 | 848.863 | 1340.270 | – | 0.470545 |
| 1905 | 4120.19 | 27.6589 | 1.685420 | 850.095 | 1361.330 | – | 0.042571 |
| 1908 | 4113.91 | 27.8155 | 1.676690 | 851.334 | 1382.400 | – | 0.020274 |
| 1911 | 4107.63 | 27.9721 | 1.667960 | 852.580 | 1403.460 | – | 0.013149 |
| 1914 | 4101.35 | 28.1287 | 1.659230 | 853.834 | 1424.520 | – | 0.010130 |
| 1917 | 4095.08 | 28.2854 | 1.650490 | 855.095 | 1445.580 | – | 0.008802 |
| 1921 | 4088.80 | 28.4420 | 1.641760 | 856.363 | 1466.640 | – | 0.008329 |
| 1923 | 4085.80 | 28.5309 | 1.642810 | 856.787 | 1476.300 | 1.4602 | 0.008264 |
| 1973 | 4063.20 | 29.4459 | 1.637270 | – | 1541.820 | 1.4402 | 0.007622 |
| 2023 | 4040.60 | 30.3609 | 1.631790 | – | 1606.490 | 1.4202 | 0.007058 |
| 2073 | 4018.00 | 31.2759 | 1.626390 | – | 1670.340 | 1.4002 | 0.006561 |
| 2123 | 3995.40 | 32.1909 | 1.621040 | – | 1733.400 | 1.3802 | 0.006119 |
| 2173 | 3972.80 | 33.1059 | 1.615750 | – | 1795.700 | 1.3602 | 0.005725 |
| 2223 | 3950.20 | 34.0209 | 1.610500 | – | 1857.270 | 1.3402 | 0.005373 |
| 2273 | 3927.60 | 34.9359 | 1.605300 | – | 1918.130 | 1.3202 | 0.005057 |
| 2323 | 3905.00 | 35.8509 | 1.600140 | – | 1978.300 | 1.3002 | 0.004771 |
| 2373 | 3882.40 | 36.7659 | 1.595010 | – | 2037.810 | 1.2802 | 0.004513 |
| 2423 | 3859.80 | 37.6809 | 1.589900 | – | 2096.680 | 1.2602 | 0.004279 |
| 2473 | 3837.20 | 38.5959 | 1.584820 | – | 2154.920 | 1.2402 | 0.004065 |
| 2523 | 3814.60 | 39.5109 | 1.579750 | – | 2212.560 | 1.2202 | 0.003870 |
| 2573 | 3792.00 | 40.4259 | 1.574690 | – | 2269.620 | 1.2002 | 0.003692 |
| 2623 | 3769.40 | 41.3409 | 1.569640 | – | 2326.110 | 1.1802 | 0.003528 |
| 2673 | 3746.80 | 42.2559 | 1.564580 | – | 2382.050 | 1.1602 | 0.003377 |
| 2723 | 3724.20 | 43.1709 | 1.559520 | – | 2437.450 | 1.1402 | 0.003237 |
| 2773 | 3701.60 | 44.0859 | 1.554440 | – | 2492.330 | 1.1202 | 0.003109 |
| 2823 | 3679.00 | 45.0009 | 1.549340 | – | 2546.710 | 1.1002 | 0.002989 |
| 2873 | 3656.40 | 45.9159 | 1.544220 | – | 2600.590 | 1.0802 | 0.002878 |
| 2923 | 3633.80 | 46.8309 | 1.539060 | – | 2653.990 | 1.0602 | 0.002775 |
| 2973 | 3611.20 | 47.7459 | 1.533880 | – | 2706.930 | 1.0402 | 0.002679 |
| 3023 | 3588.60 | 48.6609 | 1.528650 | – | 2759.410 | 1.0202 | 0.002589 |

**Table A5**: Thermophysical properties of Inconel 718 alloy in the solid state versus temperature.

| $T$ (K) | $\rho$ (kg m$^{-3}$) | $k$ (W m$^{-1}$ K$^{-1}$) | $\rho_{\mathbf{el}}$ ($\mu\Omega$ m) | $c_p$ (J kg$^{-1}$ K$^{-1}$) | $\Delta H$ (J g$^{-1}$) |
|---|---|---|---|---|---|
| 273 | 8201.01 | 10.9173 | 1.148850 | 426.084 | – |
| 323 | 8178.98 | 11.9448 | 1.166240 | 443.244 | 14.604 |
| 373 | 8156.94 | 12.9021 | 1.183600 | 452.505 | 29.465 |
| 423 | 8134.90 | 13.8030 | 1.200790 | 457.738 | 46.914 |
| 473 | 8112.86 | 14.6572 | 1.217710 | 461.897 | 66.504 |
| 523 | 8090.83 | 15.4718 | 1.234270 | 467.103 | 87.903 |
| 573 | 8068.79 | 16.2523 | 1.250400 | 474.744 | 110.856 |
| 623 | 8046.75 | 17.0031 | 1.266040 | 485.563 | 135.164 |
| 673 | 8024.71 | 17.7276 | 1.281140 | 499.752 | 160.667 |
| 723 | 8002.68 | 18.4286 | 1.295650 | 517.043 | 187.234 |
| 773 | 7980.64 | 19.1087 | 1.309520 | 536.804 | 214.756 |
| 823 | 7958.60 | 19.7696 | 1.322720 | 558.129 | 243.141 |
| 873 | 7936.56 | 20.4131 | 1.335210 | 579.928 | 272.313 |
| 923 | 7914.52 | 21.0406 | 1.346950 | 601.027 | 302.205 |
| 973 | 7892.49 | 21.6534 | 1.357910 | 620.253 | 332.758 |
| 1023 | 7870.45 | 22.2527 | 1.368050 | 636.530 | 363.922 |
| 1073 | 7848.41 | 22.8392 | 1.377360 | 648.971 | 395.654 |
| 1123 | 7826.37 | 23.4140 | 1.385800 | 656.972 | 427.913 |
| 1173 | 7804.34 | 23.9778 | 1.393350 | 660.301 | 460.666 |
| 1223 | 7782.30 | 24.5312 | 1.399970 | 659.193 | 493.880 |
| 1273 | 7760.26 | 25.0749 | 1.405640 | 654.444 | 527.528 |
| 1323 | 7738.22 | 25.6094 | 1.410350 | 647.500 | 561.584 |
| 1373 | 7716.19 | 26.1353 | 1.414050 | 640.550 | 596.026 |
| 1423 | 7694.15 | 26.6529 | 1.416740 | 636.624 | 630.832 |
| 1473 | 7672.11 | 27.1627 | 1.418390 | 639.677 | 665.984 |
| 1523 | 7650.07 | 27.6651 | 1.418980 | 654.689 | 701.464 |

**Table A6**: Thermophysical properties of Inconel 718 alloy in the liquid state and melting range versus temperature.

| $T$ (K) | $\rho$ (kg m$^{-3}$) | $k$ (W m$^{-1}$ K$^{-1}$) | $\rho_{\mathbf{el}}$ ($\mu\Omega$ m) | $c_p$ (J kg$^{-1}$ K$^{-1}$) | $\Delta H$ (J g$^{-1}$) | $\gamma$ (N m$^{-1}$) | $\mu$ (Pa·s) |
|---|---|---|---|---|---|---|---|
| 1533 | 7645.67 | 27.7647 | 1.418970 | 659.641 | 708.598 | – | 438.203000 |
| 1540 | 7622.12 | 27.8343 | 1.423850 | 663.564 | 721.661 | – | 430.428000 |
| 1547 | 7598.57 | 27.9037 | 1.428730 | 667.885 | 736.385 | – | 422.859000 |
| 1554 | 7575.02 | 27.9730 | 1.433620 | 672.624 | 752.607 | – | 415.490000 |
| 1561 | 7551.47 | 28.0422 | 1.438490 | 677.800 | 770.330 | – | 408.314000 |
| 1568 | 7527.92 | 28.1112 | 1.443370 | 683.434 | 789.552 | – | 401.324000 |
| 1575 | 7504.37 | 28.1801 | 1.448240 | 689.547 | 810.274 | – | 394.515000 |
| 1582 | 7480.83 | 28.2489 | 1.453110 | 696.162 | 832.496 | – | 387.879000 |
| 1589 | 7457.28 | 28.3175 | 1.457980 | 703.299 | 856.217 | – | 0.044285 |
| 1596 | 7433.73 | 28.3860 | 1.462850 | 710.983 | 881.439 | – | 0.014206 |
| 1603 | 7410.18 | 28.4544 | 1.467710 | 719.235 | 908.159 | – | 0.008577 |
| 1609 | 7389.49 | 28.5227 | 1.471810 | 720.000 | 933.423 | 1.88200 | 0.007610 |
| 1623 | 7382.82 | 28.6491 | 1.473530 | 720.000 | 946.367 | 1.87682 | 0.007385 |
| 1673 | 7357.17 | 29.1312 | 1.480150 | 720.000 | 994.925 | 1.85832 | 0.006608 |
| 1723 | 7331.51 | 29.6072 | 1.486770 | 720.000 | 1041.600 | 1.83982 | 0.005951 |
| 1773 | 7305.86 | 30.0773 | 1.493390 | 720.000 | 1086.470 | 1.82132 | 0.005391 |
| 1823 | 7280.21 | 30.5418 | 1.500010 | 720.000 | 1129.610 | 1.80282 | 0.004910 |
| 1873 | 7254.56 | 31.0008 | 1.506640 | 720.000 | 1171.090 | 1.78432 | 0.004495 |
| 1923 | 7228.91 | 31.4546 | 1.513260 | 720.000 | 1210.980 | 1.76582 | 0.004133 |
| 1973 | 7203.26 | 31.9033 | 1.519890 | 720.000 | 1249.350 | 1.74732 | 0.003817 |
| 2023 | 7177.61 | 32.3472 | 1.526520 | 720.000 | 1286.240 | 1.72882 | 0.003539 |
| 2073 | 7151.96 | 32.7865 | 1.533150 | 720.000 | 1321.710 | 1.71032 | 0.003293 |
| 2123 | 7126.30 | 33.2212 | 1.539780 | 720.000 | 1355.820 | 1.69182 | 0.003075 |
| 2173 | 7100.65 | 33.6516 | 1.546410 | 720.000 | 1388.610 | 1.67332 | 0.002880 |
| 2223 | 7075.00 | 34.0777 | 1.553040 | 720.000 | 1420.120 | 1.65482 | 0.002706 |
| 2273 | 7049.35 | 34.4998 | 1.559670 | 720.000 | 1450.410 | 1.63632 | 0.002549 |
| 2323 | 7023.70 | 34.9179 | 1.566310 | 720.000 | 1479.500 | 1.61782 | 0.002407 |
| 2373 | 6998.05 | 35.3322 | 1.572940 | 720.000 | 1507.450 | 1.59932 | 0.002279 |
| 2423 | 6972.40 | 35.7429 | 1.579580 | 720.000 | 1534.270 | 1.58082 | 0.002162 |
| 2473 | 6946.74 | 36.1499 | 1.586210 | 720.000 | 1560.020 | 1.56232 | 0.002056 |
| 2523 | 6921.09 | 36.5534 | 1.592850 | 720.000 | 1584.720 | 1.54382 | 0.001959 |
| 2573 | 6895.44 | 36.9535 | 1.599490 | 720.000 | 1608.400 | 1.52532 | 0.001870 |
| 2623 | 6869.79 | 37.3503 | 1.606130 | 720.000 | 1631.090 | 1.50682 | 0.001788 |
| 2673 | 6844.14 | 37.7440 | 1.612770 | 720.000 | 1652.820 | 1.48832 | 0.001713 |
| 2723 | 6818.49 | 38.1345 | 1.619410 | 720.000 | 1673.620 | 1.46982 | 0.001643 |
| 2773 | 6792.84 | 38.5220 | 1.626050 | 720.000 | 1693.510 | 1.45132 | 0.001579 |
| 2823 | 6767.18 | 38.9065 | 1.632690 | 720.000 | 1712.510 | 1.43282 | 0.001519 |
| 2873 | 6741.53 | 39.2881 | 1.639330 | 720.000 | 1730.660 | 1.41432 | 0.001464 |
| 2923 | 6715.88 | 39.6669 | 1.645980 | 720.000 | 1747.970 | 1.39582 | 0.001412 |
| 3023 | 6664.58 | 40.4164 | 1.659270 | 720.000 | 1780.160 | 1.35882 | 0.001319 |

**Table A7**: Mechanical properties of SS316L stainless steel versus temperature.

| $T$ (K) | $E$ (GPa) | $G$ (GPa) | $\nu$ | $\sigma_{0.2\%}$ (MPa) |
|---|---|---|---|---|
| 273 | 195.18 | 79.41 | 0.302561 | 305.59 |
| 323 | 194.91 | 77.02 | 0.305411 | 251.29 |
| 373 | 193.00 | 74.80 | 0.308261 | 211.29 |
| 423 | 189.92 | 72.71 | 0.311111 | 182.57 |
| 473 | 186.08 | 70.74 | 0.313961 | 162.58 |
| 523 | 181.81 | 68.85 | 0.316811 | 149.13 |
| 573 | 177.33 | 67.05 | 0.319661 | 140.41 |
| 623 | 172.82 | 65.32 | 0.322511 | 134.93 |
| 673 | 168.40 | 63.65 | 0.325361 | 131.52 |
| 723 | 164.11 | 62.04 | 0.328211 | 129.25 |
| 773 | 159.96 | 60.48 | 0.331061 | 127.48 |
| 823 | 155.90 | 58.96 | 0.333911 | 125.74 |
| 873 | 151.85 | 57.48 | 0.336761 | 123.75 |
| 923 | 147.72 | 56.04 | 0.339611 | 121.40 |
| 973 | 143.37 | 54.63 | 0.342461 | 118.68 |
| 1023 | 138.67 | 53.26 | 0.345311 | 115.67 |
| 1073 | 133.48 | 51.92 | 0.348161 | 112.53 |
| 1123 | 127.67 | 50.60 | 0.351011 | 109.42 |
| 1173 | 121.14 | 49.31 | 0.353861 | 106.53 |
| 1223 | 113.79 | 48.04 | 0.356711 | 104.00 |
| 1273 | 105.59 | 46.79 | 0.359561 | 101.91 |
| 1323 | 96.56 | 45.57 | 0.362411 | 100.25 |
| 1373 | 86.79 | 44.36 | 0.365261 | 98.89 |
| 1423 | 76.44 | 43.18 | 0.368111 | 97.54 |
| 1473 | 65.78 | 42.01 | 0.370961 | 95.75 |
| 1523 | 55.19 | 40.86 | 0.373811 | 92.82 |
| 1573 | 45.18 | 39.73 | 0.376661 | 87.84 |
| 1623 | 36.41 | 38.61 | 0.379511 | 79.61 |
| 1673 | 29.71 | 37.51 | 0.382361 | 66.63 |

**Table A8**: Mechanical properties of Ti–6Al–4V alloy versus temperature.

| $T$ (K) | $E$ (GPa) | $G$ (GPa) | $\nu$ | $\sigma_{0.2\%}$ (MPa) |
|---|---|---|---|---|
| 273 | 114.35 | 38.37 | 0.324456 | 874.40 |
| 323 | 113.39 | 37.32 | 0.323085 | 871.21 |
| 373 | 112.06 | 36.27 | 0.322975 | 854.69 |
| 423 | 110.41 | 35.22 | 0.323993 | 826.92 |
| 473 | 108.49 | 34.17 | 0.326004 | 789.84 |
| 523 | 106.32 | 33.12 | 0.328873 | 745.29 |
| 573 | 103.96 | 32.07 | 0.332467 | 694.97 |
| 623 | 101.42 | 31.02 | 0.336653 | 640.46 |
| 673 | 98.74 | 29.97 | 0.341303 | 583.22 |
| 723 | 95.96 | 28.92 | 0.346291 | 524.59 |
| 773 | 93.10 | 27.87 | 0.351498 | 465.77 |
| 823 | 90.19 | 26.82 | 0.356809 | 407.84 |
| 873 | 87.26 | 25.77 | 0.362115 | 351.77 |
| 923 | 84.32 | 24.72 | 0.367316 | 298.40 |
| 973 | 81.41 | 23.67 | 0.372320 | 248.43 |
| 1023 | 78.54 | 22.62 | 0.377045 | 202.47 |
| 1073 | 75.73 | 21.57 | 0.381418 | 160.96 |
| 1123 | 73.01 | 20.52 | 0.385380 | 124.27 |
| 1173 | 70.39 | 19.47 | 0.388881 | 92.60 |
| 1223 | 67.89 | 18.42 | 0.391887 | 66.04 |
| 1273 | 65.52 | 17.37 | 0.394377 | 44.58 |
| 1323 | 63.31 | 16.32 | 0.396345 | 28.05 |
| 1373 | 61.25 | 15.27 | 0.397800 | 16.17 |
| 1423 | 59.38 | 14.22 | 0.398772 | 8.55 |
| 1473 | 57.70 | 13.17 | 0.399305 | 4.66 |
| 1523 | 56.21 | 12.12 | 0.399462 | 3.85 |
| 1573 | 54.94 | 11.07 | 0.399330 | 5.34 |
| 1623 | 53.90 | 10.02 | 0.399011 | 8.25 |
| 1673 | 53.08 | 8.97 | 0.398634 | 11.54 |
| 1723 | 52.50 | 7.92 | 0.398347 | 14.07 |
| 1773 | 52.17 | 6.87 | 0.398324 | 14.58 |
| 1823 | 52.10 | 5.82 | 0.398762 | 11.67 |
| 1873 | 52.29 | 4.77 | 0.399885 | 3.82 |

**Table A9**: Mechanical properties of Inconel 718 alloy versus temperature.

| $T$ (K) | $E$ (GPa) | $G$ (GPa) | $\nu$ | $\sigma_{0.2\%}$ (MPa) |
|---|---|---|---|---|
| 273 | 202.39 | 77.35 | 0.291713 | 1108.20 |
| 323 | 198.94 | 77.09 | 0.293780 | 1106.97 |
| 373 | 195.53 | 76.54 | 0.291774 | 1104.87 |
| 423 | 192.16 | 75.77 | 0.287378 | 1101.52 |
| 473 | 188.83 | 74.83 | 0.281952 | 1096.53 |
| 523 | 185.54 | 73.75 | 0.276566 | 1089.43 |
| 573 | 182.29 | 72.56 | 0.272018 | 1079.72 |
| 623 | 179.08 | 71.29 | 0.268868 | 1066.91 |
| 673 | 175.91 | 69.95 | 0.267459 | 1050.49 |
| 723 | 172.78 | 68.57 | 0.267948 | 1029.94 |
| 773 | 169.69 | 67.15 | 0.270327 | 1004.83 |
| 823 | 166.64 | 65.72 | 0.274452 | 974.77 |
| 873 | 163.64 | 64.28 | 0.280070 | 939.45 |
| 923 | 160.67 | 62.85 | 0.286843 | 898.69 |
| 973 | 157.74 | 61.43 | 0.294377 | 852.47 |
| 1023 | 154.85 | 60.03 | 0.302245 | 800.94 |
| 1073 | 152.00 | 58.67 | 0.310016 | 744.47 |
| 1123 | 149.19 | 57.35 | 0.317279 | 683.69 |
| 1173 | 146.42 | 56.07 | 0.323672 | 619.52 |
| 1223 | 143.70 | 54.85 | 0.328905 | 553.20 |
| 1273 | 141.01 | 53.70 | 0.332789 | 486.37 |
| 1323 | 138.36 | 52.61 | 0.335261 | 421.09 |
| 1373 | 135.75 | 51.60 | 0.336408 | 359.86 |
| 1423 | 133.18 | 50.68 | 0.336498 | 305.72 |
| 1473 | 130.66 | 49.84 | 0.336004 | 262.28 |
| 1523 | 128.17 | 49.10 | 0.335629 | 233.74 |